CHARACTERIZING ORGANOMETALLIC-VAPOR-PHASE-EPITAXY-GROWN INDIUM GALLIUM NITRIDE ISLANDS ON GALLIUM NITRIDE FOR LIGHT EMITTING DIODE APPLICATIONS

by

Kathy Perkins Jenkins Anderson

A thesis submitted to the faculty of
The University of Utah
in partial fulfillment of the requirements for the degree of

Master of Science

Department of Materials Science and Engineering

The University of Utah

August 2011

The University of Utah Graduate School

STATEMENT OF THESIS APPROVAL

The thesis of **Kathy Perkins Jenkins Anderson**

has been approved by the following supervisory committee members:

Gerald Stringfellow	, Chair	**06/13/2011** Date Approved
Feng Liu	, Member	**06/03/2011** Date Approved
Michael Scarpulla	, Member	**06/03/2011** Date Approved

and by **Anil Virkar** , Chair of

the Department of **Materials Science and Engineering**

and by Charles A. Wight, Dean of The Graduate School.

ABSTRACT

The indium-gallium-nitride on gallium-nitride (InGaN/GaN) materials system is a promising candidate for providing a high intensity, high efficiency solution to the yet unsolved problem of solid state lighting in the range of 550 to 590 nm, a.k.a the Green Gap. The bandgap of InGaN/GaN spans the visual spectrum, making it tunable for emission at any wavelength. The lattice constant mismatch and resulting strain at the heterojunction induces a miscibility gap that enables spontaneous self-assembly of indium-rich nm-scale islands during Stranski-Krastanov growth of the InGaN active layer of the Light Emitting Diode (LED). These islands serve as quantum discs, confining excitons, and increasing internal quantum efficiency. InGaN/GaN/Al_2O_3 samples from Cao Group Inc. were interrupted after the InGaN growth step of the Organometallic Vapor-Phase Epitaxy (OMVPE) process and analyzed using Atomic Force Microscopy (AFM), High Resolution Scanning Electron Microscopy (HRSEM), Transmission Electron Microscopy (TEM), Raman, and Photoluminescence (PL) spectroscopies. Results show inhomogeneities in light emission and structure as well as conductivity. Coherence, strain, and the presence of indium were all confirmed through TEM and Energy Dispersive X-ray spectroscopy (EDX). Islands (3-10nm in height) and pits (1-4nm deep) cluster in patches with a marbled pattern. Islands tend to be found most predominantly at the edges or the bottom of pits, suggesting indium-rich island growth is

preferred along the edges of structures of high surface area, where strain from lattice mismatch is most compensated by surface area. Despite coherence, Fast Fourier Transform (FFT) reciprocal space patterns show lattice spacing and possibly the crystal structure type itself differ between island and subisland areas. The difference between island emission energy and the energy required to excite carriers is greater than expected. PL peak energy and Raman shift frequency test results were used to estimate island indium composition. Polarization of emission was observed, though was unexpected due to the InGaN having been grown on c-plane GaN which should result in isotropic biaxial strain and a valence band configuration that does not lend to bifurcating probabilities of polarization. Near-Field PL testing was performed, also with unexpected results.

CONTENTS

LIST OF TABLES

Table Page

ACKNOWLEDGEMENTS

Many people have contributed to this work. Thank you, Dr. Gerald Stringfellow, for introducing this research opportunity to me, supporting my research, and directly advising me on this project. Many thanks are also due to Dr. Densen Cao, CEO and founder of CAO Group Inc., for supplying samples and funding. Drs. Feng Liu and Michael Scarpulla dedicated time to answer my questions and helped to guide the development of my understanding on this subject. Dr. Xiaobin Niu further exercised my understanding of diffraction patterns and their modeling. It was Dr. Loren Reith of the U of U Nano Surface Science Lab who introduced me to my first nano-scale image of the surface of our first sample. From the U of U Physics Dept., Drs. Matthew Delong, Randy Polson, John Lupton, and Sebastian Bange spent many hours capturing and interpreting spectroscopic images. From the BYU Physics Dept., Dr. Richard Vanfleet and Felipe Rivera also dedicated much time and resources to imaging and evaluation.

Acknowledgement is also due to the many authors who published the work referenced in this paper, with special mention to those who gave their permission that their figures be reprinted here. Thanks to Kelly Harward for closely reviewing the manuscript format. And, of course, my exploration into this subject would not have been possible without the support of my husband, David Anderson. Many thanks are due to him, and to my sons Jared and Gregory for their support, encouragement, and enormous patience.

1 BACKGROUND

1.1 Introduction

Artificial lighting directly affects quality of life, but comes at a cost that is not sustainable at current usage rates and with the present mix of lighting device technology used, considering the rising cost of electricity and the environmental impact of producing that electricity. World lighting energy consumption results in greenhouse gas emissions equivalent to 75% of world car emissions *(1)*. The U.S. Lighting Market Characterization Report prepared for the US Dept. of Energy, and published in 2002, estimates US energy consumption for lighting at that time was 765TWh per year, the cost of which was on the order of $80 billion. Incandenscent lamps consumed 42% of that energy, while providing only 12% of the total light produced. Less than 1% of lamps reported were solid state devices, and those were strictly in crosswalk and traffic signal use *(2)*. However, light emitting diodes can match or exceed the performance of incandescents and even fluorescents with respect to both light output and energy efficiency. It is an emerging technology with the potential for use in almost every lighting application. Solid state lighting presents a viable means for mitigating rising utility costs and the environmental impact of keeping the lights on when we need them.

1.2 Advantages of Light Emitting Diodes

When comparing the function of common artificial light sources, it is easy to see why light emitting diodes (LEDs) are more efficient. While incandescent lamps function by heating a highly resistive filament until it emits some light as well as heat, LEDs experience negligible thermal energy loss. Fluorescent lamps excite mercury vapor to produce Ultra-Violet (UV) light, which then excites a phosphor to emit light in the lower energy, visible range of the spectrum. Converting UV to visible light results in an energy loss dissipated thermally. By comparison, LEDs can emit monochromatic light in the visible spectrum with negligible thermal energy loss. And, while the currently marketed white LED technology presents LEDs that convert UV or blue light to white light by embedding a high-energy-emitting LED in a matrix of lower-energy-emitting phosphors (Figs 1-1 and 1-2), emerging advances are showing such a conversion may be unnecessary. White light can be achieved by combining LEDs that directly emit monochromatic red, green, and blue.

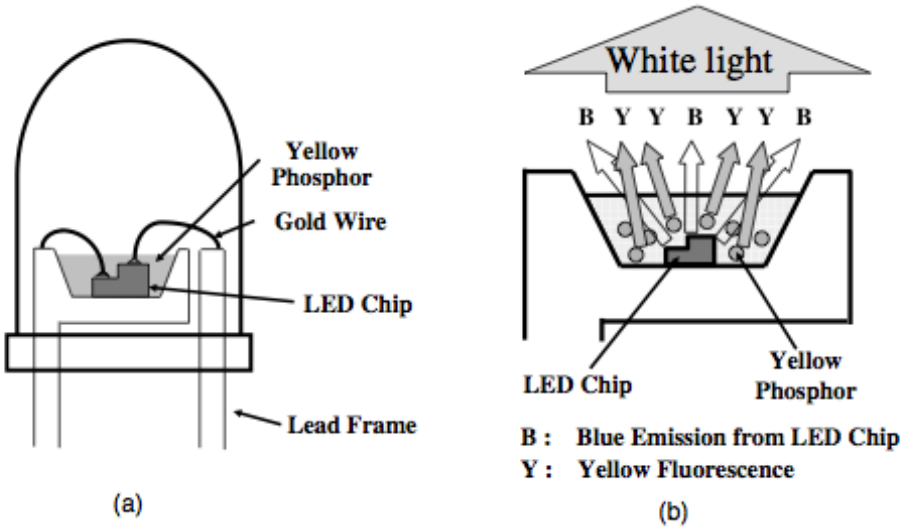

Figure 1-1 Spectra of the Ultra-high R_a White LED, the Conventional White LED, and CIE standard Illuminates (D_{50}). Reprinted with permission from Yukio Narukawa *(3)*.

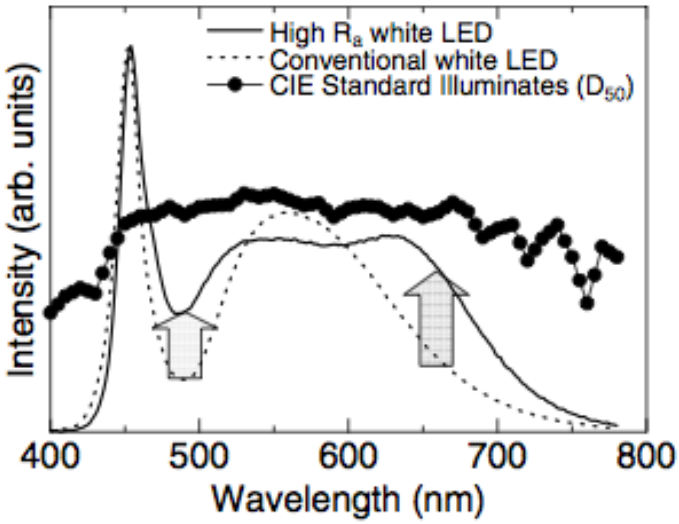

Figure 1-2 Spectra of the ultra-high R_a white LED, the conventional white LED, and CIE standard illuminates (D_{50}). Reprinted with Permission from Yukio Narukawa *(3)*.

1.3 Principle Function and Structure of Light Emitting Diodes

Aptly named, an LED is a semiconducting diode, directing DC current in a single direction between positive and negative terminals or contacts. Within the semiconductor are layers of highly ordered crystalline materials (Fig 1-3), the compositions of which are designed to direct the flow of carriers of electric charges through the device. The diode requires a negatively doped (n-type) layer with an excess of electrons, and a positively doped (p-type) layer with a deficit of electrons, separated by a nondoped emissive layer or layers, designed for radiative recombination of excited carriers where electrical potential is converted to photons and light is emitted spontaneously. The most narrow energy gap between the emissive layer's conduction and valence bands determines the wavelength of light emitted (Fig 1-4).

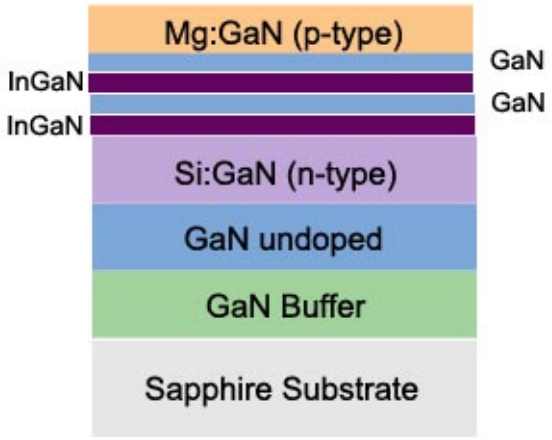

Figure 1-3 InGaN/GaN LED Material Layers

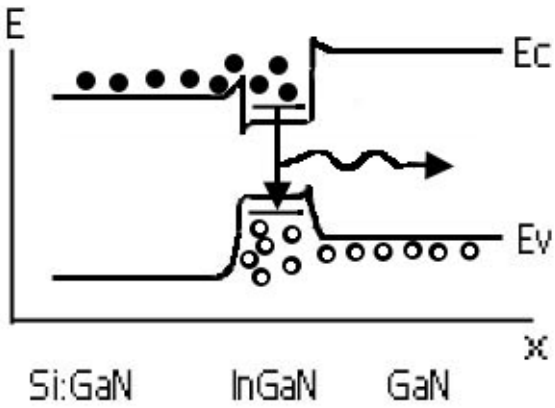

Figure 1-4 Energy Band Diagram of Si:GaN/InGaN/undoped GaN

1.4 Calculating Efficiency

The LED's most influential advantage over other lighting technologies is its efficiency. Internal quantum efficiency (IQE), $\eta_{int,}$ is the ratio of radiative recombination rate to total recombination rate, representing the success ratio of conversion of carrier current to photons.

Eq. 1

$$\eta_{int} = \frac{R_r}{R_{r+}R_{nr}} = \frac{\tau_{nr}}{\tau_{nr}+\tau_r}$$

Here, R_r and R_{nr} are rates of radiative and nonradiative recombination, respectively, and τ_r and τ_{nr} are the lifetimes of charge carriers before radiative and nonradiative recombination. Nonradiative recombination occurs at defect sites in the crystal structure, dissipating energy into the lattice as phonons, heating the device. With this relationship, it is apparent that maximizing nonradiative recombination lifetime, and minimizing radiative recombination lifetime, are essential to maximizing internal quantum efficiency.

External quantum efficiency (EQE), η_{ext} is a multiple of IQE and the optical efficiency, representing the conversion of carrier current to photons that are not internally absorbed or captured by internal reflection, but that successfully escape the device.

Eq. 2

$$\eta_{ext} = \eta_{int}\eta_{opt}$$

Internal reflection and absorption are minimized by both packaging geometry design and choice of materials according to their refractive and absorptive properties.

Luminous efficiency, η_{lu}, is the figure of merit used when comparing different lighting technologies. It takes into account relative eye sensitivity, and is expressed in units of lumens/watt (lm/W).

Eq. 3

$$\eta_{lu} = \frac{683 \int V(\lambda) P_{op}(\lambda) d\lambda}{VI}$$

Over the span of 150 years, the incandescent bulb's luminous efficiency, which is also sometimes referred to as luminous efficacy, has evolved from 1.5 to 16 lm/W. Fluorescent lamp technology presented a leap forward, starting with a luminous efficiency of 50 lm/W and, over several decades, achieving a plateau of 100 lm/W. By contrast, white LED efficiency has improved roughly 30x per decade, overtaking its competitors, achieving 150 lm/watt, and continues to rise (Fig 1-5) *(3)*.

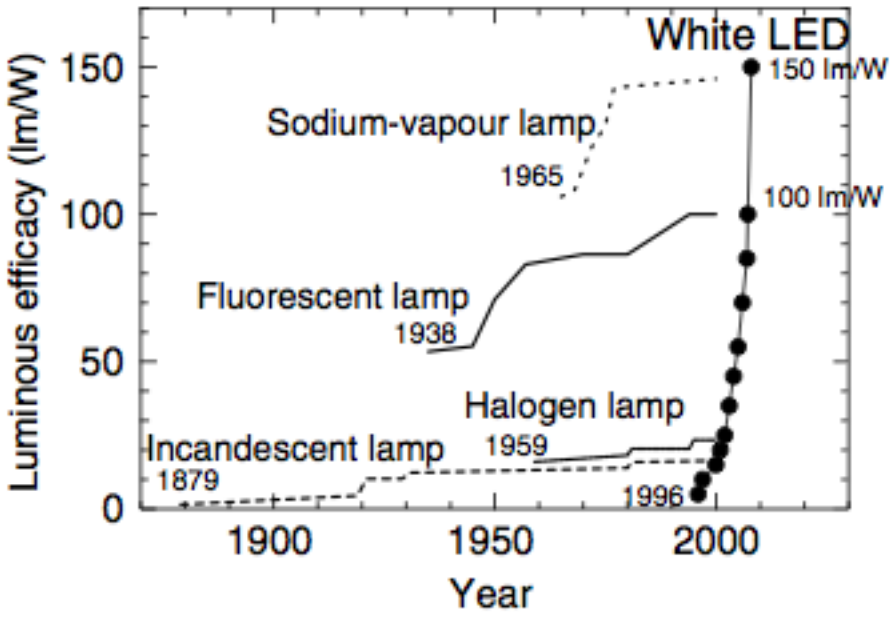

Figure 1-5 The History if η_{lu} in Incandescent Lamps, Halogen Lamps, Fluorescent Lamps, Sodium-vapor Lamps, and Commercial White LEDs. Reprinted with Permission from Yukio Narukawa *(3)*.

In order for any new lighting technology to issue a significant response from the lighting market, consumers require that they be both cost-effective and emit a spectrum the human eye cannot easily distinguish from the solar spectrum. The spectral comparison is made by evaluating the color quality of the device, referred to as its chromaticity.

Chromaticity specifies values for the red, green, and blue (RGB) components of any color, including white (Fig 1-6) *(4)*. The white point of an sRGB display, for example,

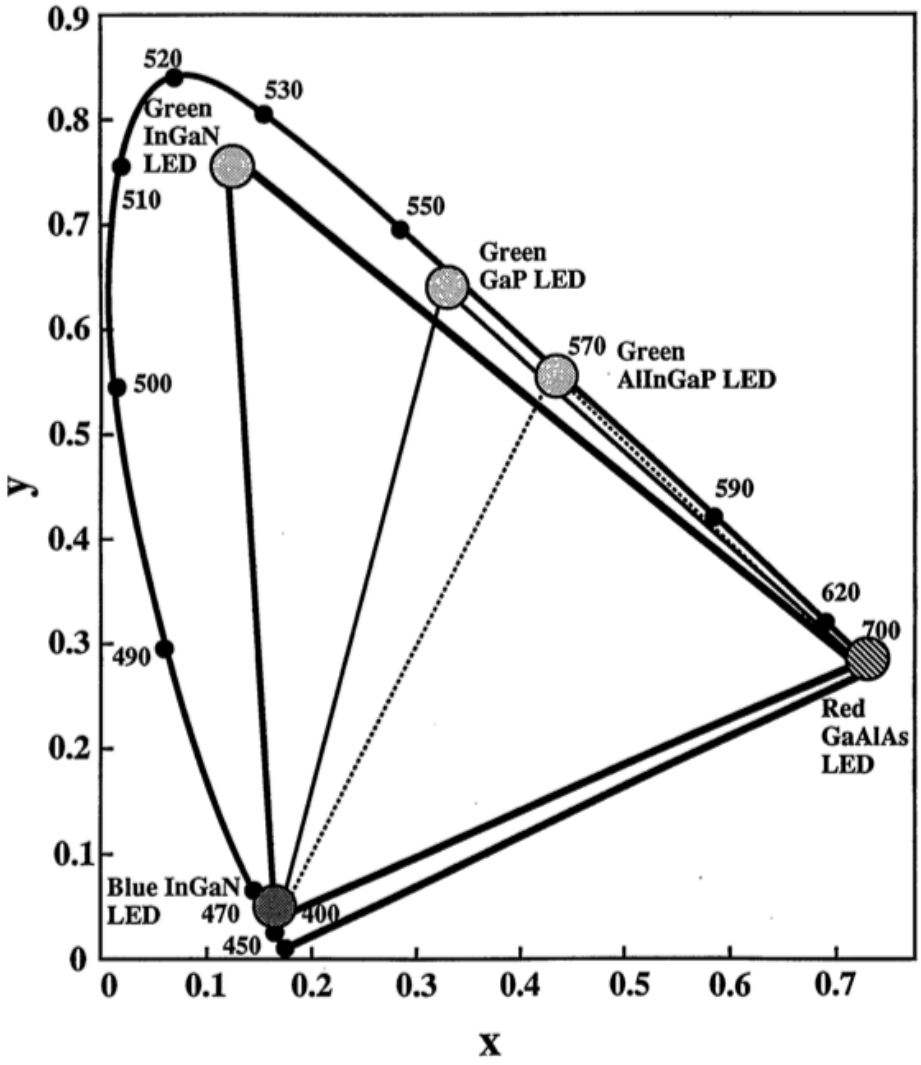

Figure 1-6 Chromaticity. Reprinted with permission from Shuji Nakamura *(4)*.

has an x,y chromaticity of [0.3127,0.3290]. When at the white point, reducing the contribution of any one of the RGB light sources results in an off-white light that seems unnatural to the human eye. Efficiently achieving a solar-like spectrum is a challenge that LEDs have previously failed to meet, due to the historical poor-to-none external quantum efficiency exhibited in the wavelength range from 525 to 625nm *(5)*, commonly referred to as the Green Gap.

1.5 InGaN/GaN Material System Advantages

1.5.1 Bandgap Tunability and Bond Strength

As an alloy, InGaN has a bandgap that can span the entire visible spectrum (Fig 1-7) *(6)*. Because emission wavelength is directly related to bandgap, this means $In_xGa_{1-x}N$ presents a single-alloy-system theoretically capable of spontaneously emitting all three primary wavelengths, RGB, that are required to directly produce a chromatically true white LED. Using a single alloy rather than a duo or trio of alloys simplifies, and therefore reduces, the time and cost of fabrication.

Cathodoluminescence test results show increasing emission wavelength with increasing In composition, proving tunability (Fig 1-8) *(7)*.

Like its components, InN and GaN, InGaN is a direct-bangap material, radiatively recombining carriers without paying an energy penalty to momentum change. This poses a significant advantage in the efficiency equation.

The high bond strengths of InN and GaN (Table 1-1) make the InGaN alloy degradation-resistant under high current density. This enables a wide operating temperature range, and a long lifetime for reliability of InGaN-based devices.

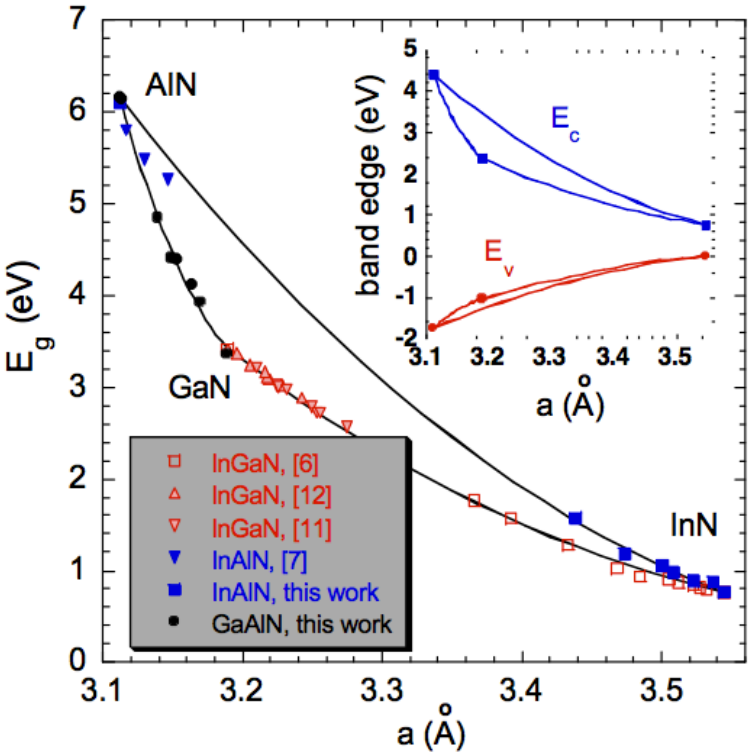

Figure 1-7 Bandgap and Bandedge vs Composition of InN, AlN, and GaN System. Reprinted with Permission from Wladek Walukiewicz *(6)*.

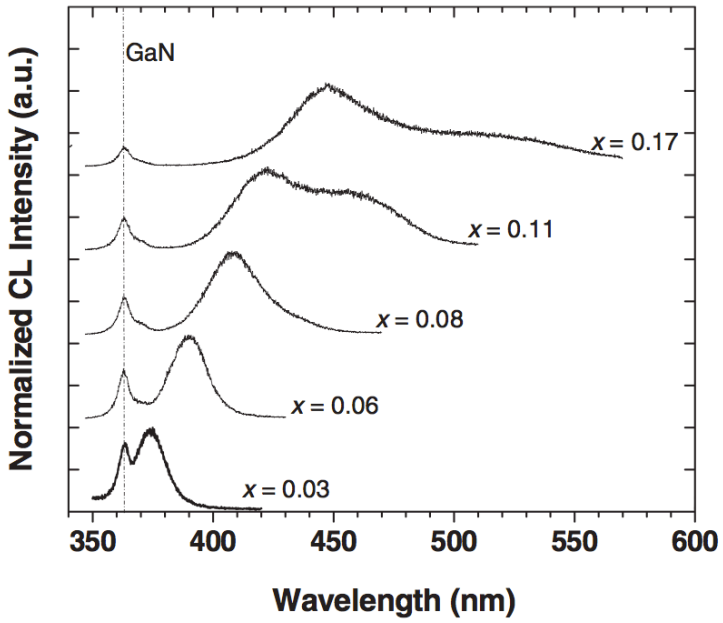

Figure 1-8 Cathodoluminescence vs Indium Composition. Reprinted with Permission from Fernando Ponce *(7)*.

Table 1-1 Bond Energies of Common Semiconductors

System	*Bond Energy (ev/atom)*
GaN	8.92 *(8)*
InN	7.72 *(8)*
AlN	11.52 *(8)*
Si-N	355 kJ/mol *(9)*
Si-Si	222 kJ/mol *(9)*
Si-C	318 kJ/mol *(9)*

1.5.2 Wurtzite Crystal Structure

As III-V compounds, both GaN and InN bond tetrahedrally, resulting in two possibilities for their crystal structure: wurtzite *(10)*, which has two interpenetrating hexagonal repeat units; and zincblende, which has two interpenetrating face-centered-cubic repeat units. Decades of historical observation have found wurtzite (Fig 1-9) to be the most stable phase for each.

While cubic structures have three directions of symmetry, the wurtzite crystal structure can only have two. The significance of this becomes apparent when considering crystal polarity and the dynamics of strain.

The Fractional Ionic Character (FIC) of GaN and InN bonds (0.51 and 0.54, respectively *(11)*) builds into the wurtzite crystal structure a net polarity in the c direction. Crystal polarity with respect to the direction of injection current flow in the LED affects emission energy as well as electron-hole wavefunction overlap. InGaN grown in a direction of no or low crystal polarity, also referred to as nonpolar and semipolar (grown on a, m, or r planes rather than c plane), results in a higher

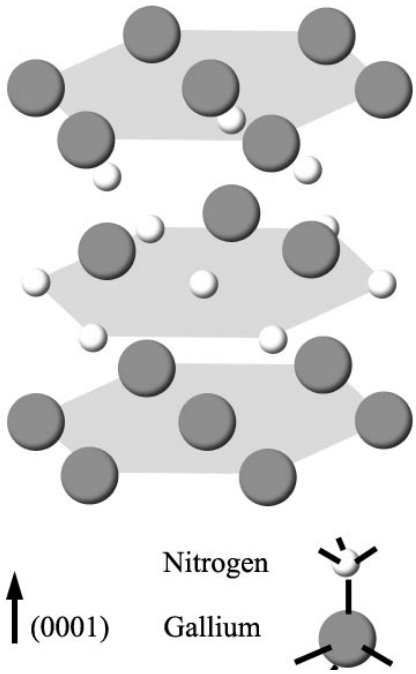

Figure 1-9 Wurtzite Crystal Structure

photoluminescence (PL) emission energy in the growth direction due to reduced losses attributed to the polarity-induced electric field, also known as the Quantum Confined Stark Effect (QCSE). Because the QCSE is also responsible for a reduced electron-hole wavefunction overlap, minimizing the QCSE should reduce radiative recombination lifetime, thereby increasing IQE. However, these advantages do not come without a cost. With present growth processing techniques, defect densities in a and m plane-grown GaN and InGaN are higher than in c plane, resulting in lower IQE and EQE due to higher defect-related nonradiative recombination *(12)*. With respect to choosing non- or semipolar growth over c-plane, the only other reported potential advantage that could overcome the presently observed increase in defect density would be an increase in indium incorporation that could increase InGaN SK island density and provide more radiative recombination centers for charge carriers as competing alternatives to the

nonradiative ones. A 32% increase in indium incorporation was observed by De Mierry et al. when comparing InGaN QW compositions that were simultaneously grown, in the same process chamber and batch run, on semipolar (11$\bar{2}$2) vs c-plane (0001) GaN on sapphire substrates *(13)*.

Strain in the c-plane, also referred to as biaxial strain, can affect both emission energy and polarization. Compressive biaxial strain increases bandgap, increasing PL emission energy. When this strain is isotropic, emission is not polarized. However, when the strain is anisotropic, and all three lattice constants differ ($a_1 \neq a_2 \neq c$), valence bands are split, introducing a difference in the probability any given photon emitted will be polarized in the parallel vs perpendicular direction. Detecting PL emission polarization from samples grown on 0001 GaN requires capturing and analyzing emission from edge geometries. Edge geometry PL measurements enable clear distinction between QW and QD-like device characteristics *(14)*.

1.6 Strain, Defects, and Self-Assembly

Lattice parameter mismatch between InN and GaN (Table 1-2) introduce strain at the InGaN/GaN heterojunction and in the growing InGaN layer, resulting in a large, positive enthalpy of mixing and miscibility gap *(15)*. Without an avenue for strain relief, indium incorporation in the InGaN layer, at an epi growth temp of less than 700K, should theoretically be limited to less than 1% (Fig 1-10) *(16)*.

Bulk InGaN films grown with higher indium content than is miscible exhibit evidence of spontaneous phase separation and/or high defect densities, with indium clustering at defect sites. This behavior would seem to inhibit the possibility of targeting a wide range of indium compositions to enable tuning InGaN LED emission wavelength across the

Table 1-2 Lattice Parameters and Coefficients of Thermal Expansion of Sapphire, InN, and GaN

Room Temp	*c (nm)*	*a (nm)*	*α_a (1e-6/K)*
Sapphire	1.0298	.4765	7.5
GaN	.5185-.5186	.3188-.3189	5.6
InN	.569-.576	.353-.358	3.6

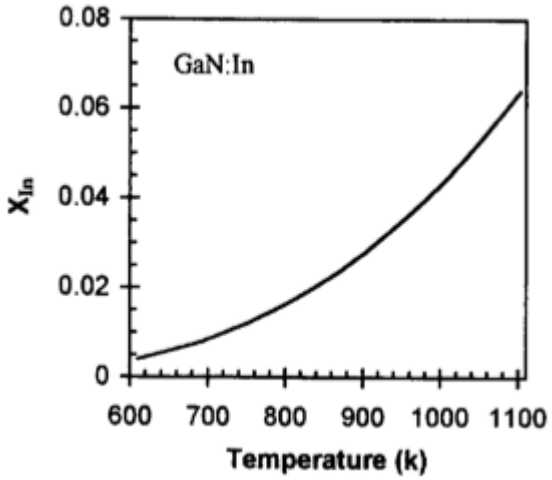

Figure 1-10 Calculated Solubility Limit of In in GaN vs Temperature. Reprinted with permission from Ihsiu Ho *(16)*.

visible spectrum. However, failure to acknowledge what appeared to be the limit of miscibility led to experiments with results that suggested an unexpected solution. Engineering strain into the epi growth process can affect the temperature and composition conditions required for miscibility of InN in GaN. This was illustrated by Karpov et al., in their publication of an InGaN phase diagram with an asymmetric binode and spinode that, when compared with a phase diagram of relaxed InGaN, is shifted toward the InN-

rich side of the diagram *(17)*. This means that, as higher compressive strain in a coherent InGaN layer is achieved, higher indium incorporation is possible.

Higher indium incorporation is not the only significant advantage of strained epitaxial growth of InGaN. An equal if not more influential benefit of strained growth is the tendency of strained thin films to transition from 2D to 3D growth, independently forming nano-scale structures with highly useful properties, the most important of which is the phenomenon making IQE of devices with 3D grown structures less susceptible to defect density than 2D grown thin films. This is crucial because, due to extreme lattice mismatch, growing GaN on sapphire results in defects on the order of $10^8/cm^3$, a density that is transferred to the InGaN layer during growth. It is a defect density that would render an LED of any other system inoperable. This phenomenon to which the seemingly defect-impervious nature of 3D-grown InGaN is attributed, is the localization of excitons by coherent, indium-rich islands of a height, after capping , less than the Bohr radius of an exciton (2.8nm for GaN). Exciton localization provides preferred, lower bandgap recombination centers that increase the radiative recombination rate. When island density exceeds defect density, the exciton localization effect successfully overcomes defect-directed nonradiative recombination, thereby preserving a significant portion of the IQE.

Epitaxial growth of an element or alloy can be modeled in one of three modes: Van der Merwe, Stranski-Krastanov, or Volmer Weber, with distinctions between them made according to the magnitude of biaxial strain at the interface (a lengthier explanation can be found in section 3.5.16 of Morkoc *(24)*). In the case of InGaN growth on GaN, the growth mode is said to be Stranski-Krastanov, where a 2D wetting layer is formed and

builds in height. As the film height increases, so does the total compressive strain energy within the film until it reaches a critical value beyond which the strain inhibits further 2-D monolayer growth of uniform composition. Large indium adatoms, while encountering a substrate lattice with smaller spacing than strain-free InN, have a choice between paying a high cost for adsorption at an already strained, flat surface, and a lower cost for adsorption at a step edge, void edge, or other nonflat surface. These adatoms prefer the lower energy cost of adsorption, thereby initiating, then propagating, 3D growth. As adsorption of indium and gallium continues, and as InN has a larger relaxed lattice parameter, and therefore a stronger aversion to 2D growth in this case than GaN, islands increase in indium concentration as they grow in size. As the epi growth process is mass-transport-rate limited, growth configuration does not achieve equilibrium, meaning it is unable to rearrange to a more thermodynamically stable order before being locked into place.

Successfully achieving Stranski-Krastanov growth requires a level of control of process conditions that is a significant challenge to the Organometallic Vapor Phase Epitaxy (OMVPE) crystal growth system. These conditions include, but are not limited to, precursor and substrate temperature, growth time, gas flow patterns at the surface of the substrate, pyrolysis of precursors, and the ratio of flows of Ga and In precursors with respect to each other, and with respect to the flow of Nitrogen source. The sensitivity of this process is well evidenced by a recent study (2011) by Falta et al. who found that, for an In/(In + Ga) flux ratio of 0.74, and a growth temp of 700°C, no islands were observed. However, introducing a post-InGaN growth anneal time of 1 minute resulted in quantum-dot-like features that emit at 2.75eV, and then extending the postgrowth anneal to 5

minutes results in the loss of those features and their associated emission *(18)*. Outside a very small window of allowed process condition limits, epi growth is not coherent for $In_xGa_{1-x}N$ where $x > 0.06$, but is either a) overwhelmed with new defects or b) exhibits phase separation.

In the case of new defects (independent from the defects already propagating from the GaN layer beneath), these defects form as strain-relief centers. Not only does their relief of strain interfere with the goal of increasing InN miscibility with increasing compressive strain, but they also add to the density of nonradiative recombination centers, thereby reducing IQE.

In the case of phase separation within a planar film, the InGaN layer grows with composition limited according to the strain-free phase diagram of InGaN. Build-up of strain is prevented by the formation of μm-scale pockets of mostly InN surrounded by a matrix of mostly GaN, with phase boundaries between. In this case, not only do the phase boundaries serve as nonradiative recombination centers, reducing IQE, but the InN rich regions collect the vast majority of any surviving charge carriers, where they radiatively recombine at a low energy in the IR rather than in the desired visible spectrum.

Achieving Stranski-Krastanov growth not only protects IQE through exciton localization and redraws the limits of the the InN:GaN miscibility gap, restoring the possibility of engineering InGaN composition for light emission to span the visible spectrum, but it also adds the advantage of self-assembly, as the spontaneously formed indium-rich islands are of nm-scale which is a smaller size than would be achievable through lithography. Useful nano-scale patterning without lithography poses a

tremendous fabrication cost advantage. Island size, composition, and density can be engineered by controlling epi process conditions, thereby tuning emission wavelength and intensity.

1.7 Quantum Confinement

Quantum confinement is achieved when feature size, L_x, is less than the Bohr radius of an exciton *(19)*. For GaN, this is about 2.8nm.

Eq. 4

$$Bohr\_radius_{ex} = \frac{\hbar}{\sqrt{2m_{ex}E_{ex}}} \approx 2.8nm$$

Excitons are localized to within the feature volume. As compared to what would be expected from a bulk material, the density of electron energy states in a feature of quantum confinement size is reduced, and bandgap is increased according to the following *(19):*

Eq. 5

$$E_{QC} = \frac{h^2}{8}\left(\frac{1}{m_x d_x^2} + \frac{1}{m_y d_y^2} + \frac{1}{m_z d_z^2}\right)$$

With the increase in bandgap comes an increase in emission energy, thereby increasing IQE. This is illustrated in Fig 1-11, where emission intensity is plotted against energy for three different sized MBE grown InGaN/GaN QDs *(20)*.

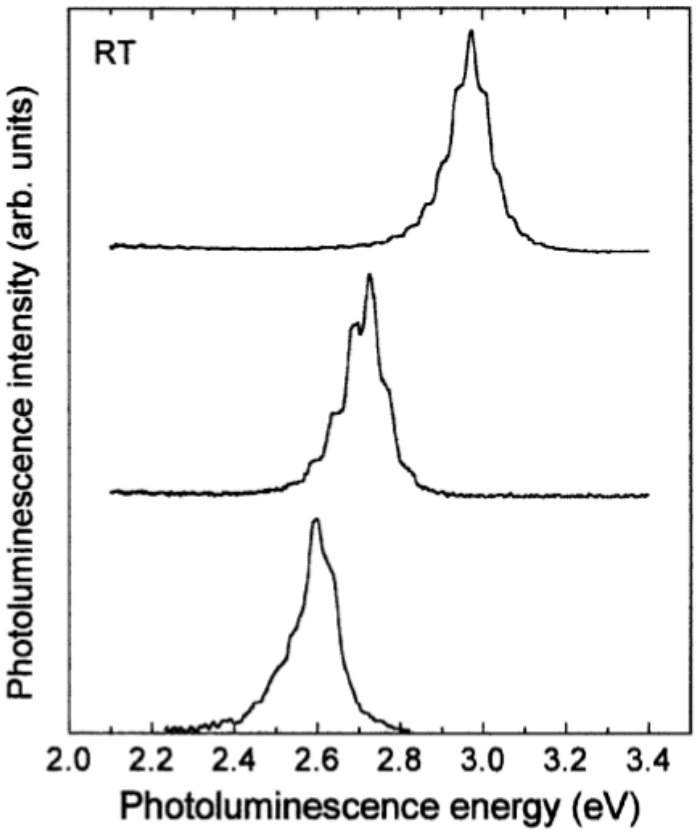

Figure 1-11 RT PL of InGaN QDs of different sizes: 1.5, 2, and 3 nm corresponding to energies of 2.97, 2.71, and 2.60 eV, respectively. Indium composition is reportedly 15% in each case. Reprinted with permission from Jean Massies *(20)*.

2 MOTIVATION

Bringing new LED technologies to market requires a process control system that will minimize losses incurred at each process involved. Effective process control requires a working model of the process, something not yet achieved for the SK growth of InGaN islands on GaN, and will require the following:

- Finding a technique for measuring indium distribution at a sampling volume resolution on the order of the size of an SK-grown island.
- Identifying useful characterization methods including an approach to isolate relationships between device performance, materials properties, and dominant fabrication process variables.
- Developing a pool of reliable, useful benchmark data.

3 CAO GROUP SAMPLES

3.1 Sample Preparation

Two samples were provided by Cao Group Inc, an Optoelectronics corporation headquartered in West Jordan, UT. Each sample consisted of an uncapped, OMVPE-grown InGaN layer of approximately 2.5nm (10ML), grown on 2.3 micron n-type (Silicon doped to 5e18/cm3) GaN, grown on 1.5 micron undoped GaN, grown on a low temp (LT) buffer layer, grown on a 2" c-plane sapphire substrate (Fig 3-1). The bulk dopant concentration of 5e18/cm3 of the n-type GaN layer provides an interface Si concentration of 1e10/sqcm.

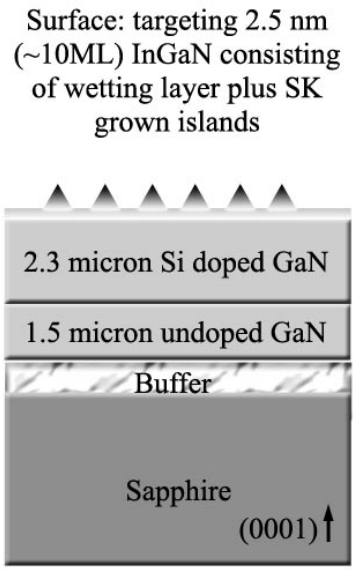

Figure 3-1 Cao Samples Configuration

3.2 Analysis Techniques and Objectives

Our objective in this study was to correlate the surface topography of these samples with composition and optical properties. The techniques chosen were the following:

- Atomic Force Microscopy (AFM) for surface topography
- High Resolution Scanning Electron Microscopy (HRSEM) for a supporting topographical perspective, as well as to view whether conductivity patterns corresponded with AFM patterns such as island density.
- High Resolution Transmission Electron Microscopy (HRTEM) to verify coherence, compare island and subsurface diffraction patterns, and estimate strain.
- Coincident Raman Spectroscopy, AFM, and Photoluminescence (PL) to map and correlate inhomogeneities in composition gradients, topography, and emission characteristics.
- Electron Energy Loss Scanning Transmission Electron Microscopy (EELS STEM) to quantify indium composition in islands and between them.

In successfully employing the above techniques, commonalities between topography, composition, and emission characteristics can be observed, and compared to an existing theoretical model of SK growth.

4 SAMPLE ANALYSES AND RESULTS

4.1 AFM and Topography

With the assistance of Dr. Loren Reith, U of U Nano-Surface Science Lab[1], an Atomic Force Microscope (AFM) was used in tapping mode to scan the surface of the samples and record changes in z height with respect to x and y position. WSxM software *(21)* was used to plot the data into maps, isolate significant areas of those maps, and render them 3D.

4.1.1 AFM Sample 1

Sample 1 has islands and pits, their densities on the order of e^{8} and e^{10} per cm^2, respectively (Fig 4-1). Large hillocks are also present, their density on the order of 1 per μm^2. Island height ranges from 3 to 25 nm, and is typically 10nm (Table 4-1). Islands are more frequently found at the edges and bottoms of pits, than in isolation (Fig 4-2). Some pits are elongated, resembling trenches, with adjacently aligned islands that form ridges (Fig 4-3). Pits are asymmetrical, with walls of differing angles (Fig 4-4).

[1] Raw AFM scans of Sample 1 were captured by Dr. Loren Reith, Nano-Surface Science Lab, University of Utah.

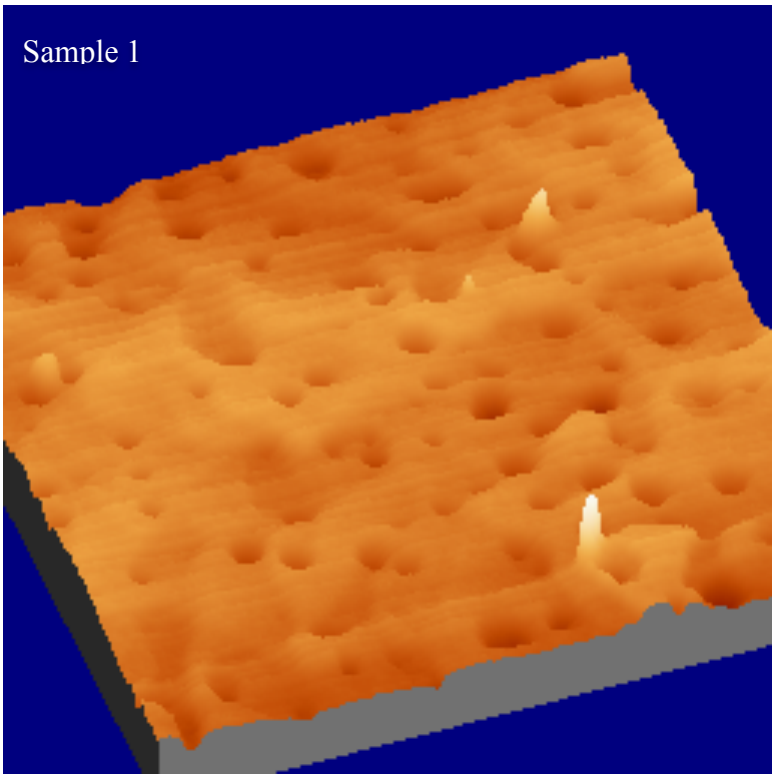

Figure 4-1 AFM scan of pits and islands, Sample 1 (see footnote 1 page 22).

Table 4-1 Sample 1 Topographical Statistics from AFM Scans

	Sample 1
Island Density	$3e^{8}$ cm^{-2}
Island Height	3 to 25 nm (typically 10nm)
Island Diameter	40 to 300 nm
Pit Density	$1e^{10}$ cm^{-2}
Pit Depth	1 to 4 nm
Pit Diameter	50 to 140 nm

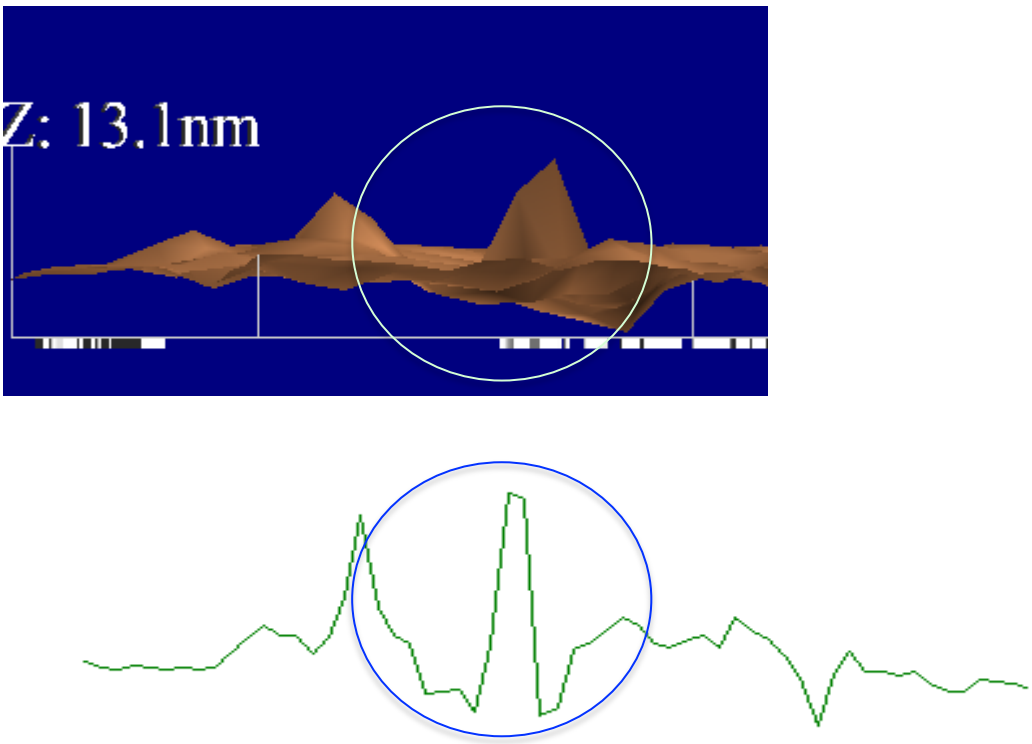

Figure 4-2 Topographical View (top) and Linear Profile (bottom) of an Island in the Base of a Pit (see footnote 1, p 22)

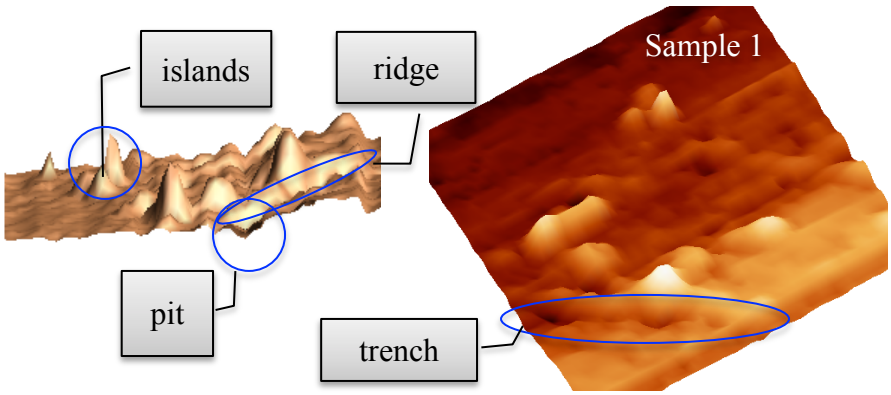

Figure 4-3 Two views of the same AFM scan of 2umx2um area of Sample 1. Islands, ridge, trench, and incline of surface are shown. Z-height from lowest to highest points in this image is 33nm. These islands range from 8 nm high, 200nm wide, to 25nm high, 350nm wide. These pits are about 5nm deep (see footnote 1, p 22).

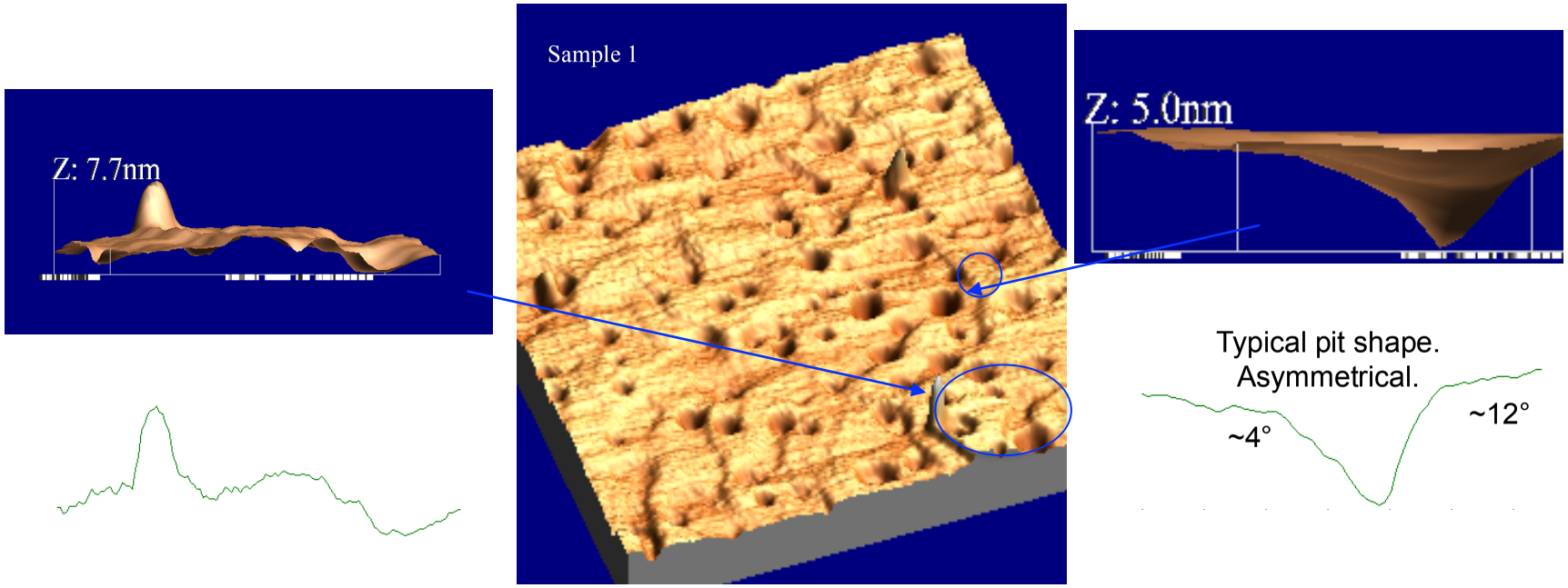

Figure 4-4 Topographic and Profile Views of Islands and pits; b) Asymmetrical pits; and c) Islands at the edges of pits (see footnote 1, p 22).

4.1.2 AFM Sample 2

Sample 2 has no islands and no pits (Fig 4-5). Two possibilities to explain this are either:

1) SK islands grew to the point of coalescence.
2) 2D growth did not transition to 3D.

4.2 HRSEM: Islands, Pits, and Inhomogeneity

High Resolution Scanning Electron Microscope (HRSEM) images of Sample 1 were captured by Dr. Matt DeLong, U of U Physics Dept, using an FEI Novanano 630[2]. In these gray-scale images, areas of higher conductivity appear brighter.

Inhomogeneities of differing conductivity were recognized, appearing on the order of 5 micron, and in a marbling pattern (Fig 4-6).

Semiconductor conductivity is directly proportional to dopant concentration and charge mobility. In an n-type semiconductor such as Si:GaN and the InGaN layer grown

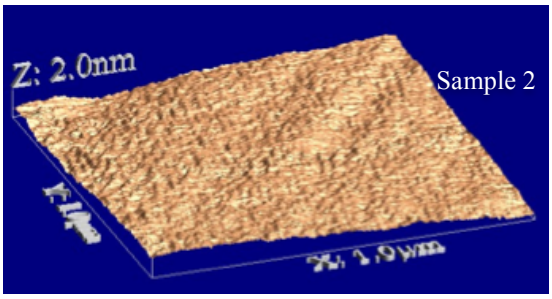

Figure 4-5 AFM scan of Sample 2; smooth surface

[2] High Resolution Scanning Electron Microscope (HRSEM) images of Sample 1 were captured by Dr. Matt DeLong, U of U Physics Dept, using an FEI Novanano 630

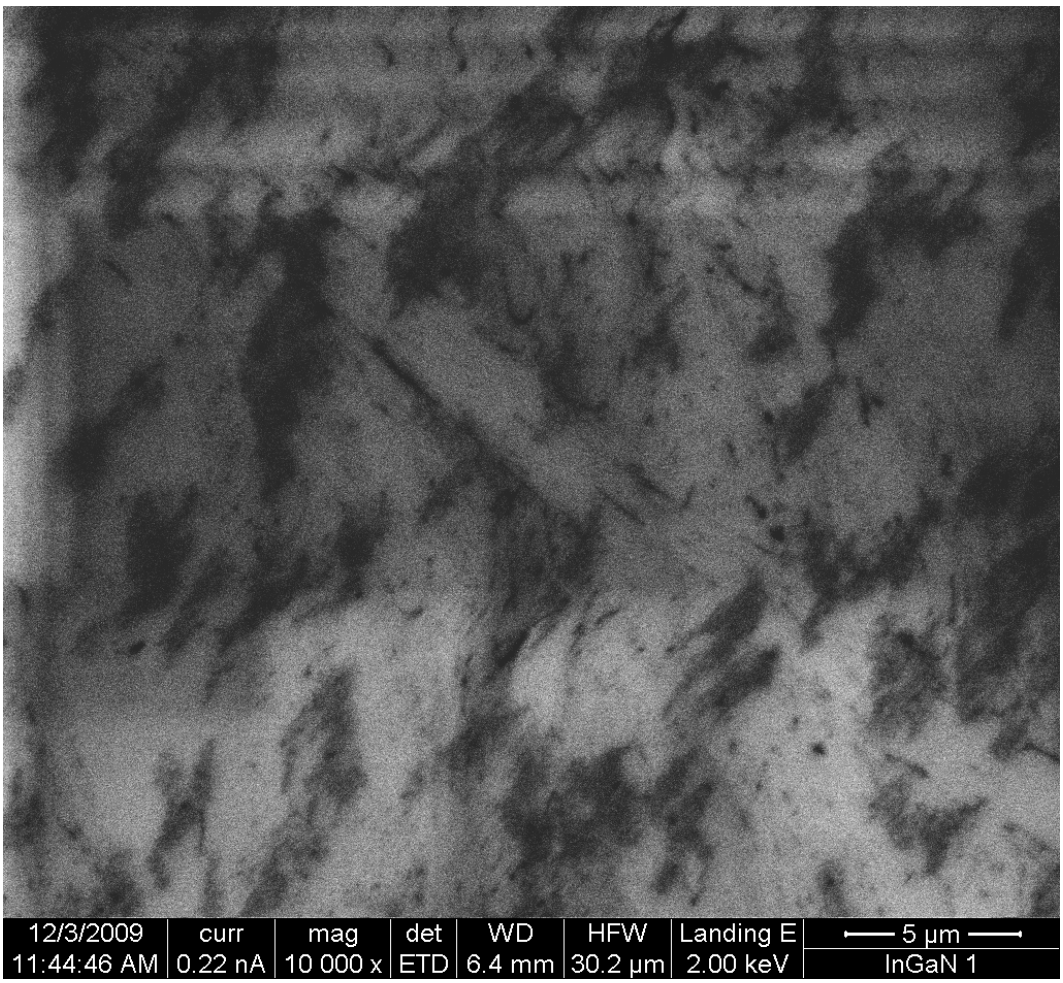

Figure 4-6 Surface conductivity inhomogeneity in marbling pattern revealed by HRSEM of Sample 1.

above it, this relationship can be represented as *(22)*:

Eq. 6

$$\sigma = q\mu_n n$$

The electron mobility of GaN at 300K is known to be 1400 cm^2/V *(24)*, but finding the electron mobility of InN for a direct comparison is more difficult. However, a comparison is still possible through the relationship between drift velocity, v_d, and low-field mobility, μ_0 *(22)*:

Eq. 7

$$v_d = \frac{\mu_0 \mathcal{E}}{\left[1 + \left(\frac{\mu_0 \mathcal{E}}{v_s}\right)^{c_2}\right]^{1/c_2}}$$

Foutz et al., in 1999, published velocity field characteristics of wurtzite InN, GaN, and AlN. In that study, the drift velocity of InN was shown to be significantly greater (starting at 3x) than that of GaN for electric fields in the range of zero to 100kV/cm, then again for 200kV and above *(23)*. Because drift velocity for InN is greater than for GaN, per the above relation, mobility must be as well, and it can be reasonably assumed that InN is more conductive than GaN. Therefore, with respect to the micro-scale conductivity inhomogeneities shown in the HRSEM images, if dopant concentration is uniform and there are no other causes of carrier inhomogeneity, it is likely that the dark areas are InN-poor, and light areas have a higher InN concentration.

In Fig 4-7, small, highly conductive dots are seen, often surrounded by a slightly larger, nonconductive area. The diameter range of these dots is consistent with the diameter range of islands as measured from preceding AFM images of the same sample. Because indium is more conductive than gallium, it is expected that these highly conductive dots are indium, and the dark spots that surround many of them are pits. Island density and pit density are not consistent over all areas of the sample. Some pits contain islands, and some are vacant. Some areas as wide as 50x50 micron have no islands (Fig 4-8), some have no pits, and still others have neither.

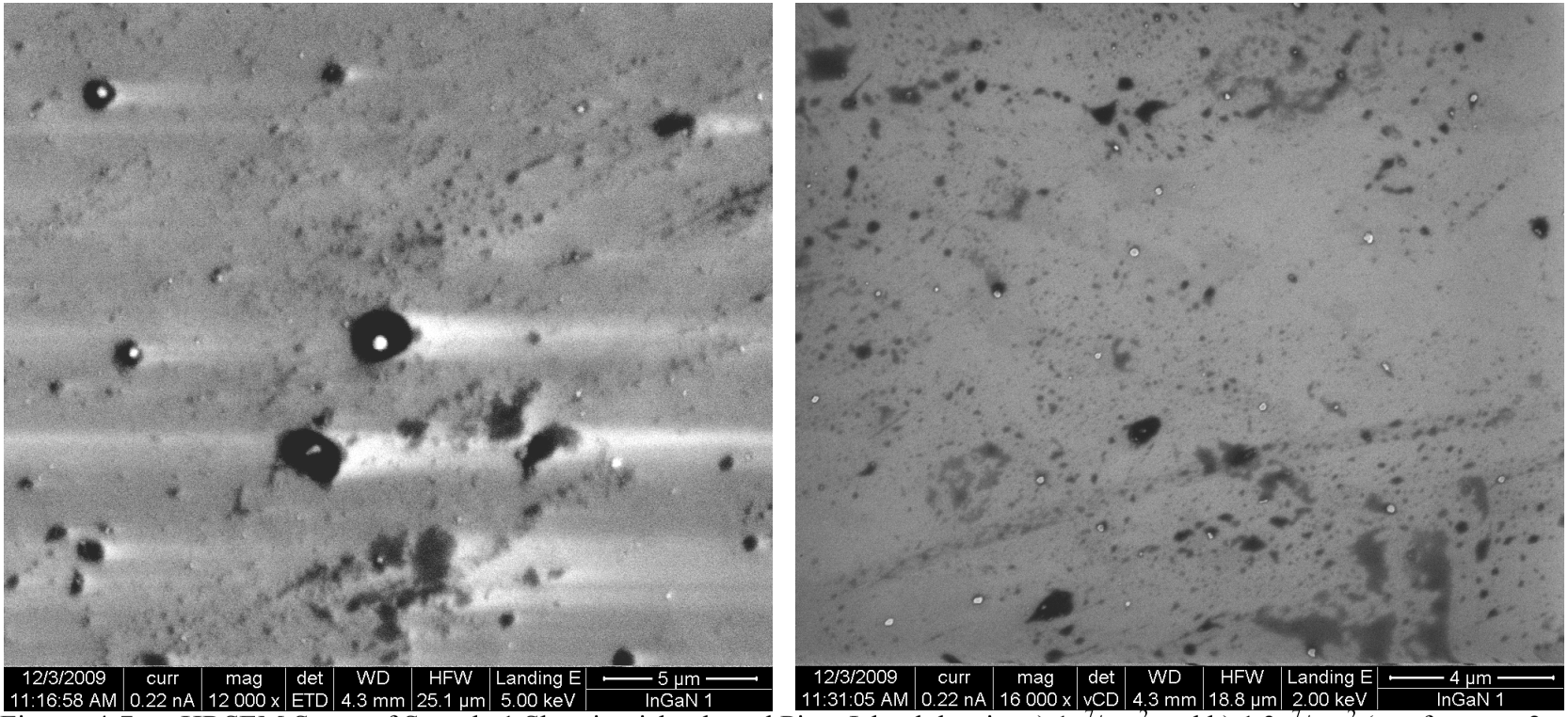

Figure 4-7 HRSEM Scans of Sample 1 Showing islands and Pits; Island density a) $1e^{7}/cm^{2}$ and b) $1.3e^{7}/cm^{2}$ (see footnote 2, p 26).

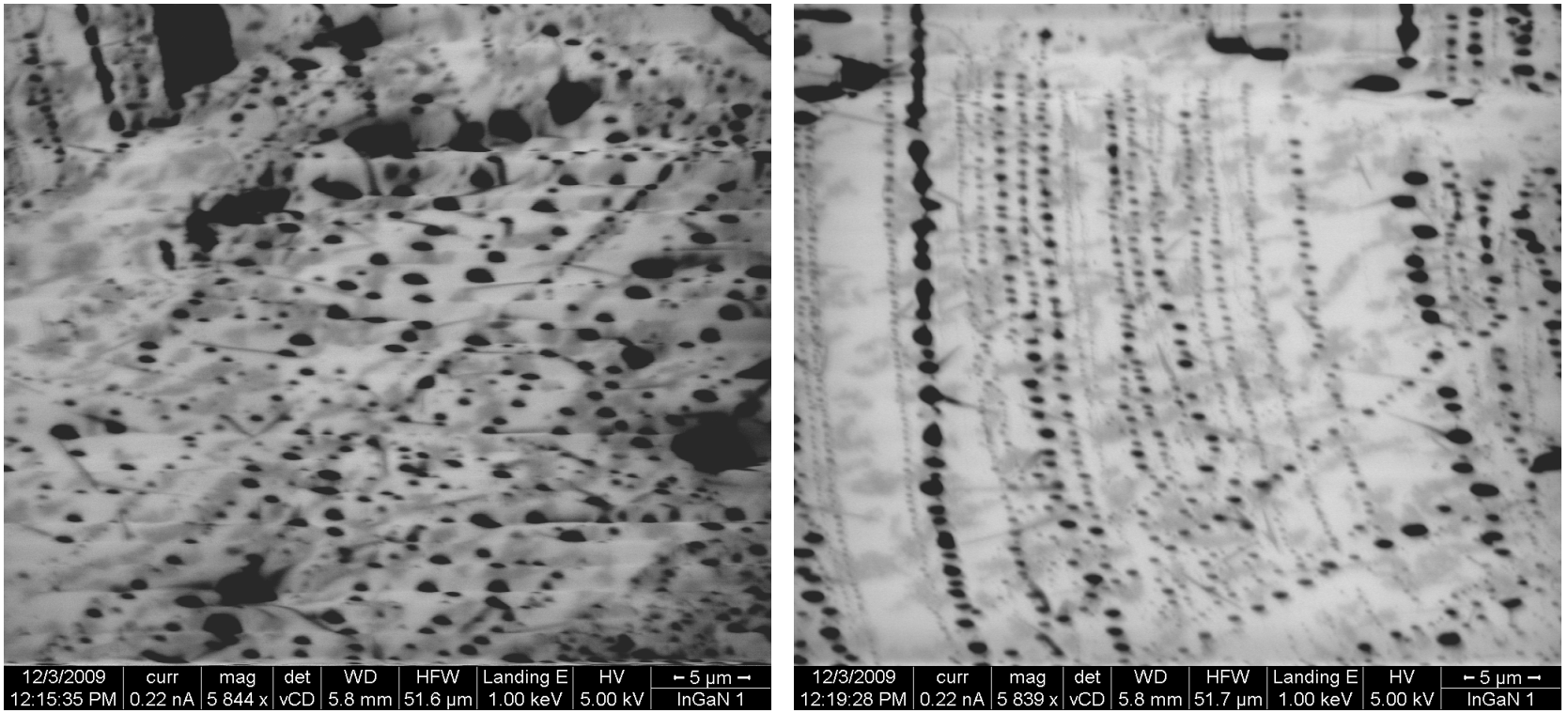

Figure 4-8 HRSEM of Sample 1 showing no islands, but the presence of both conductivity inhomogeneities and pits of varying sizes, some pits without pattern, some pits in trails, some trails in parallel, and some trails intersecting (see footnote 2, p26).

4.3 HRTEM

Two islands from Sample 1 were cross-sectioned by Drs. Felipe Rivera and Richard Vanfleet of the Brigham Young University Physics Dept.[3] who captured High Resolution Transmission Electron Microscope (HRTEM) images of each island cross-section to confirm coherency. No defects, grains, or grain boundaries were observed at the interfaces (Fig 4-9). Fast Fourier Transform (FFT) reciprocal space patterns confirmed crystallinity in both the island and the GaN beneath it (Fig 4-9 insets). While the diffraction pattern for the GaN beneath the island is clearly consistent with wurtzite GaN, the crystal structure and orientation of the island is not as easily understood.

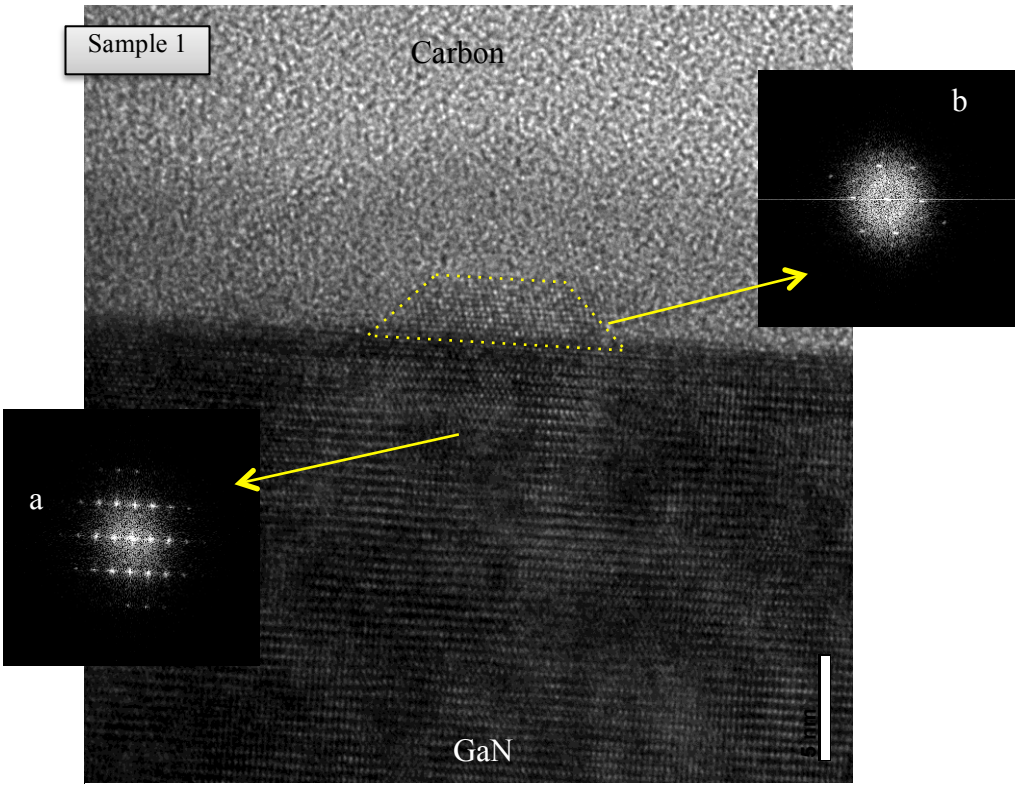

Figure 4-9 Real-space HRTEM Image of Sample 1, Cross-section 1 with Insets: FFT Reciprocal Space Patterns of a) Subisland GaN and b) Island 1 InGaN

[3] HRTEM images, FFTs, and EDX measurements are shown with permission from Drs. Richard Vanfleet and Felipe Rivera, Brigham Young University Physics Dept.

Energy Dispersive X-ray spectroscopy (EDX) was performed for Island 1, and the presence of indium confirmed (Fig 4-10). Integration of EDX peaks for In and Ga estimate the indium:Ga composition ratio at this spot of the island shown in part a of Fig 4-10 to be 15:85. By this same method, the ratio at another island spot was estimated to be 45:55.

Because the confidence level of EDX composition assessment for structures of this size is small, a more quantitative approach to indium composition measurement will require a different analysis technique.

Reciprocal space lattice space values (Fig 4-11) were measured from the FFT patterns and used to calculate real space lattice spacings, both in the island and the GaN beneath it. Resulting values, when compared with published nonstrained c and a lattice constants, proved subisland GaN to be tensile (Tables 4-2 and 4-3). Consequently, in order to achieve coherency and maintain a force balance, the island, at the interface, must be compressive.

Subisland (GaN) lattice spacings were found to be larger than published values for unstrained GaN. The diffraction pattern of Island 1 showed two different lattice spacings, neither of which are consistent with c-lattice spacing of wurtzite GaN, InN, or InGaN. EDX showed no other elements that are not already typical of the HRTEM environment. The nearest match in lattice spacings between island and subisland is for the m lattice constant.

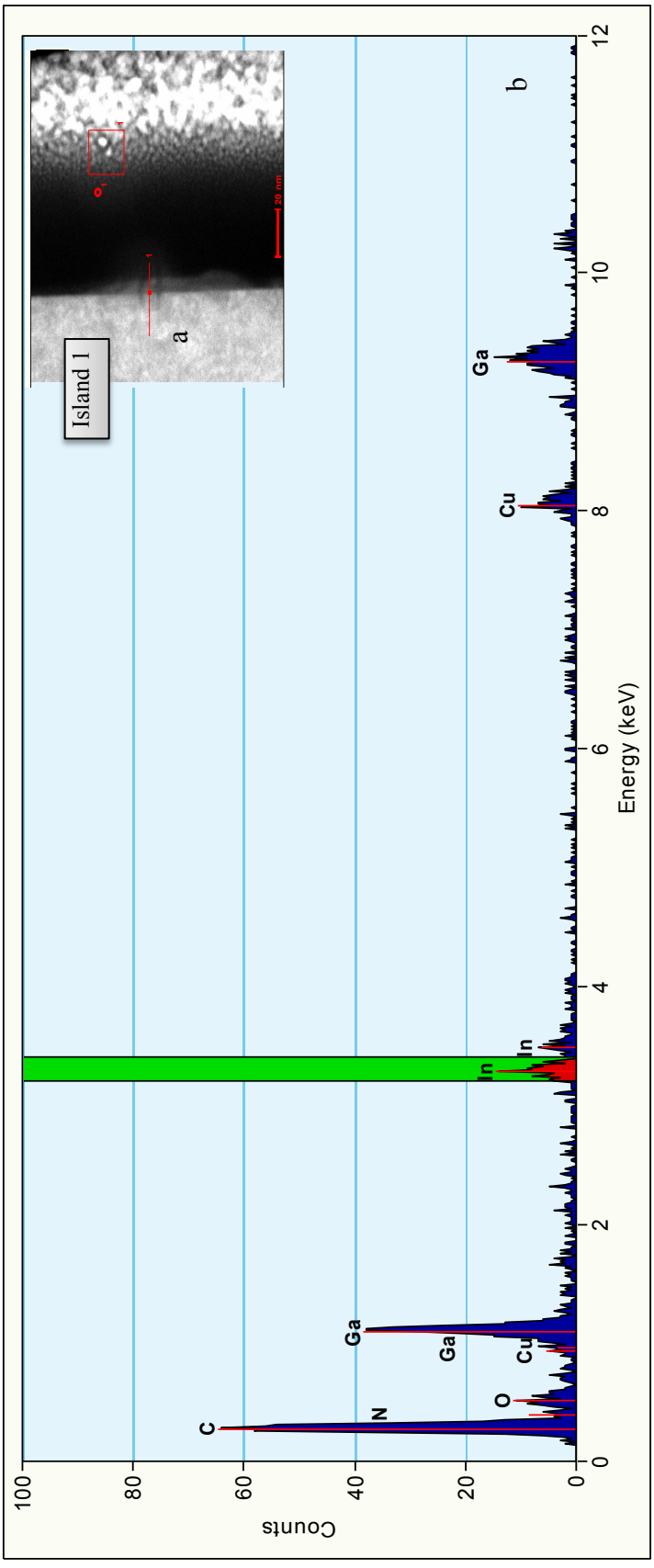

Figure 4-10 HRTEM EDX a) real-space x-section of island and b) EDX of that island in the location marked 1 (see footnote 3, p **Error! Bookmark not defined.**).

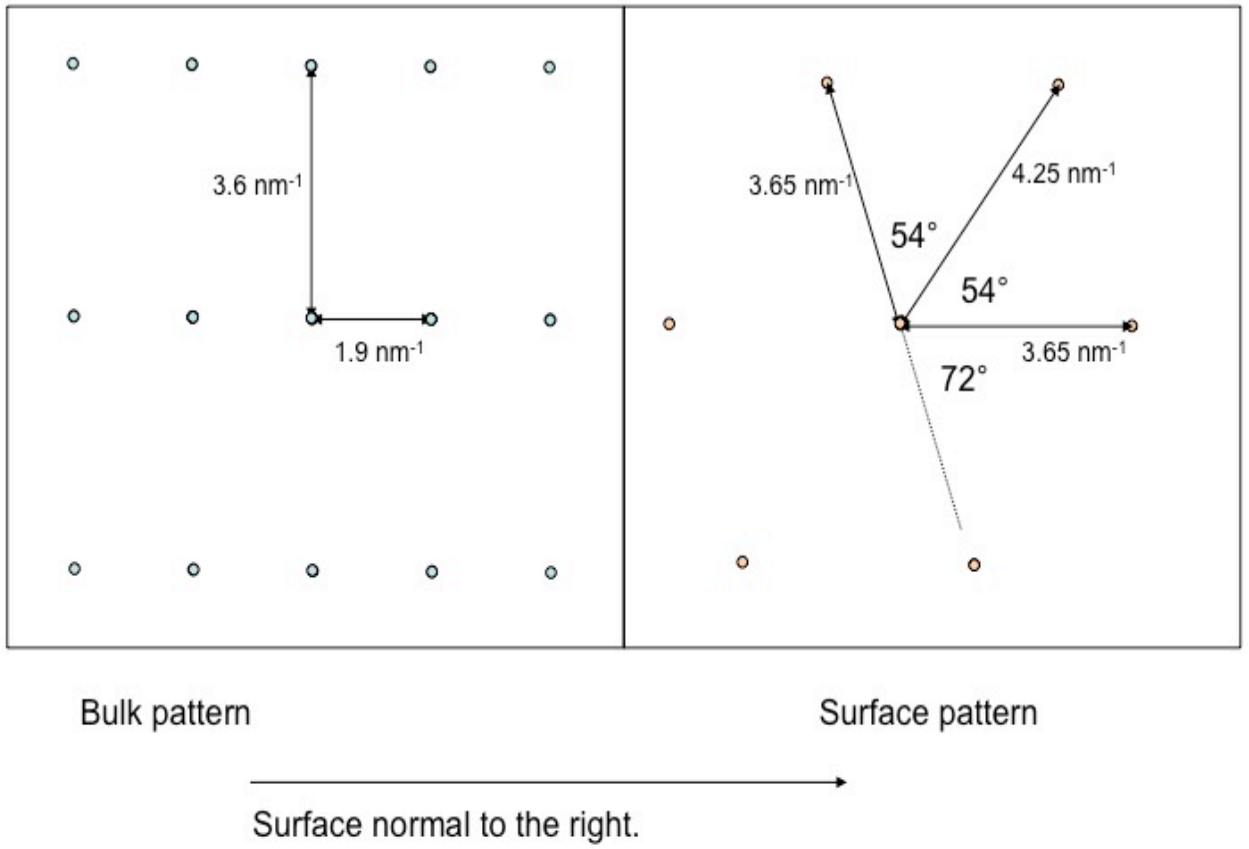

Figure 4-11 Lattice spacing derived from FFT Diffraction Patterns, Sample 1, x-section 1 (see footnote 3, p **Error! Bookmark not defined.**).

Table 4-2 FFT-Derived Lattice Spacings Island and Subisland, Sample 1, X-section 1, Island 1

Subisland GaN	*Island 1 InGaN*
c = 0.5263 nm	d_1 = 0.2353 nm
m = 0.2777 nm	d_2 = 0.2740 nm
a = 2m/√3 = 0.3208 nm	

Table 4-3 HRTEM Measured Strain, Sample 1

*Lattice Parameter**	*Unstrained InN (nm)***	*Unstrained GaN (nm)***	*Sample 1 Subisland (nm)*	*Sample 1 Island (nm)*
a_w	.353±.001	0.3188±.0001		0.2740 if W and on side Least likely
m_w	.305±.001	0.2761±.0001	0.2777 tension, 0.58% strain	
c_w	.573±.004	0.5185±.0001	0.5263 tension, 1.50% strain	
a_z	0.498	0.4511±.01		0.47 if ZB Matches, but also not likely

**Subscripts w and z correspond to wurtzite and zincblende crystal structures, respectively*

***Standard nonstrained lattice parameter values taken from Morkoc, Handbook of Nitrides and Semiconductor Devices, Vol 1, 2008 (24)*

Beneath both islands, tensile strain in the growth (0001) direction is 1.5%, which is more than 10x the tensile strain expected in that direction for bare GaN grown on sapphire. This expectation was formed according to a 2010 study by Zhang et al. *(25)* who used High Resolution X-ray Diffraction (HRXRD) and PL measurements to find that a 3.3μm layer of GaN, OMVPE-grown on a 20nm LT GaN buffer layer, which was grown on c-plane sapphire, to have a strain in the growth direction and at room temp of 8.2e-4, which is tensile and less than 0.1%. The GaN layers (the sum of both undoped and doped layers) for Samples 1 and 2 were approximately 3.8μm, 15% thicker than the 3.3μm layer evaluated by Zhang.

For Island 2, a real space image was used for measuring lattice spacing of both island and subisland (Fig 4-12). Resulting values correspond reasonably well with localized area FFT-derived values for lattice spacings of Island 1 and the GaN beneath it (Table 4-4). This supporting evidence using a separate island reduces the likelihood that the unusual lattice spacing measured from Island 1 was an artifact of the measurement technique.

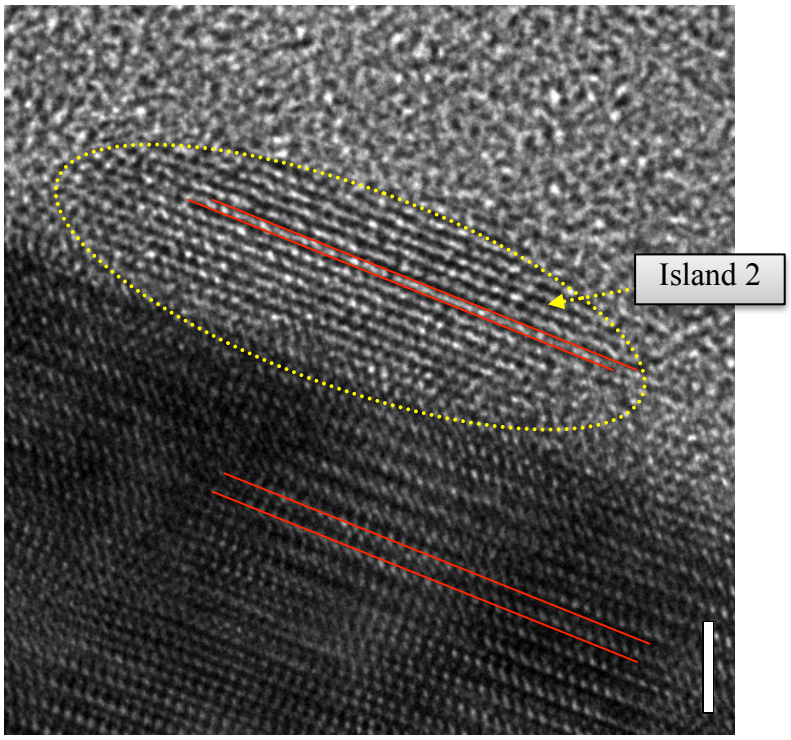

Figure 4-12 HRTEM Real-space Image of Sample 1, Island 2 (see footnote 3, p 31)

Table 4-4 Real-space HRTEM Image Measurements of Lattice Spacing Support FFT-derived Data

	GaN			*InGaN*	
Lattice Constant	Subisland 1 FFT-Derived Values	Subisland 2 Real-Space Image Value	Lattice Spacing	Island 1 FFT-Derived Values	Island 2 Real-Space Image Value
c (nm)	0.5263	0.52	d_2 (nm)	0.2740	0.29

4.3.1 Using Measured Strain to Estimate PL Emission Energy for GaN

With an understanding of the difference between bandgap and excited carrier recombination emission energy, the bandgap can be used to estimate or predict emission energy of excitons beneath the islands during their recombination, a useful reference for interpreting PL data. Once composition and crystal structure are known, the strain-free, nondoped low temp bandgap can be found in published literature. However, there remain three other factors to be considered when calculating bandgap: temperature, dopant concentration, and strain.

Using the Varshni equation to account for the effect of temperature*(26)*:

Eq. 8

$$Eg(T) = E_0 - \frac{\alpha T^2}{T + \beta}$$

with E_0 = 3.505 eV, and linear and nonlinear fitting parameters, alpha and beta for GaN equalling 3.75e-4 eV/K and 270 K, respectively *(27)*, the bandgap of unstrained, undoped, room temp (RT) GaN was calculated to be 3.45 eV. Luong Tien et al. *(28)* experimentally found the RT FXA PL emission energy from GaN to be 3.43eV, which is 20meV lower than value calculated from the above Varshni equation. A similar calculation for InN with E_0 = .690 eV and using values for alpha and beta of 0.414 meV/K and 454 K, respectively, *(29*) results in a RT bandgap for InN of 0.641 eV.

Dopant concentration has also been reported to affect bandgap according to the relationship *(30)*:

Eq. 9

$$\Delta Eg(n) = -K(n^{\frac{1}{3}} + p^{\frac{1}{3}})$$

This relationship is referred to as the bandgap renormalization effect, where K for GaN was found by RT photoreflectance measurements to be (2.4±0.5)e-8 eV. Considering the islands of Sample 1 were grown on Si:GaN of 5e18/cm3, the corresponding bandgap shift in the upper GaN layer, attributable to dopant concentration, is -0.12 eV.

The GaN bandgap for unstrained 5e18/cm3 Si:GaN at RT is therefeore 3.45 – 0.12 = 3.33 eV. This estimate is lower than the 3.40eV value for emission from unstrained, RT Si:GaN found by interpolating between experimantal PL values measured by Schubert et al. corresponding to dopant concentrations of 3 and 7e18/cm3 *(31)*.

The effect of Sample 1's subisland strain on the bandgap of GaN was estimated to be 0.213eV using the relationship *(25)*:

Eq. 10

$$E_g(\varepsilon_\perp) = E_g(0) + b_{g\perp}\varepsilon_\perp \ (eV)$$

where $\varepsilon_\perp$ represents the strain perpendicular to the c-plane, or $(c_{actual}\text{-}c_0)/c_0$, and $b_{g\perp}$ = 14.2 eV. According to the quasicubic approximation *(32)*:

Eq. 11

$$\varepsilon_\perp/\varepsilon_\parallel = -\frac{2C_{13}}{C_{33}} = -0.689$$

the blueshift effect of a tensile strain perpendicular to the c-plane corresponds to the blueshift effect of a compressive biaxial strain (strain parallel to the c-plane), $\varepsilon_\parallel$:

Eq. 12

$$E_g(\varepsilon_{\parallel}) = E_g(0) + b_{g\parallel}\varepsilon_{\parallel}\ (eV)$$

where $b_{g\parallel}$ = -5.5 eV for $\varepsilon_{\parallel} < 0.25\%$, and $b_{g\parallel}$ = -13 eV for $\varepsilon_{\parallel} > 0.25\%$ *(33)*. According to this relationship, the effect of Sample 1's subisland strain on the bandgap of GaN is –0.075eV.

Whether these relationships developed using studies of 2D thin films and quantum wells are applicable to the 3D grown system and its nonplanar, noncontinuous strain fields remains to be tested. In this study, as an approximation, we assume that the above $E_g(\varepsilon_{\parallel})$ relationship holds true, despite the subisland GaN having been measured to be tensile in both the uni-axial and biaxial directions, and therefore not compliant with the quasicubic approximation.

This brings the total Eg of the GaN directly beneath the islands to be 3.45 – 0.12 - 0.075 = 3.255 eV, which is at least 75meV lower than the surrounding GaN. With an estimated island density of 3e8/cm2, and a typical diameter of 50nm, the ratio of subisland to free-surface GaN is .024, or about 2%. Despite this, the radiative recombination expected from the GaN should still be significantly affected by the subisland strain. This is because excitons in the GaN are not trapped in quantum confinement structures, as are the excitons in the islands. Therefore, if an exciton in the GaN with a free surface (no island above it) can diffuse to an area of tensile in-plane strain (an area directly beneath an InGaN island), then it will be swept into and recombine at that lower bandgap region.

If the free-surface GaN is not strain-free, but compressively strained as would be expected from the entire GaN surface before any islands were grown, then the bandgap for these GaN areas is 3.45 – 0.12 + 0.0142 = 3.34 eV.

Therefore, considering temperature, dopant concentration, and strain, the range of emission energies predicted for GaN during photoluminescence testing is between 3.255 and 3.34 eV, the extremes representing subisland and free-surface areas, respectively.

4.4 Photoluminescence

Wide-area PL spectra were collected using two independent equipment configurations. Data collected by and shown here with the permission of Drs. John Lupton and Sebastian Bange, U of U Physics Dept.[4], were collected by exciting the samples using an excitation source approaching the InGaN layer from above (from the surface). Additionally, Randy Polson, also of the U of U Physics Dept.[5], used a Witec alphaSNOM near-field optical microscope to collect emission after excitation of the sample from below (from the substrate).

As seen in Figs 4-13 and 4-14, emission spectra from Sample 1 collected from the two independent test configurations have a common peak, the highest intensity peak of each spectrum, at 3.0± 0.07 eV.

The test performed with the 349 nm (3.56 eV) excitation source (Fig 4-14) resulted in emission peaks at 2.95, 3.05, 3.30, and 3.38 eV. The two highest energy peaks fall mostly within the prediction that the energy range of GaN emission would be between 3.255 and 3.34 eV. These UV peaks at 3.30 and 3.38 eV correspond with biaxially

[4] PL data collected by Drs. Sebastian Bange and John Lupton, University of Utah Physics Dept., are shown with their permission.
[5] PL data collected using the Witec alpha tool were collected by Dr. Randy Polson, U of U Physics Dept.

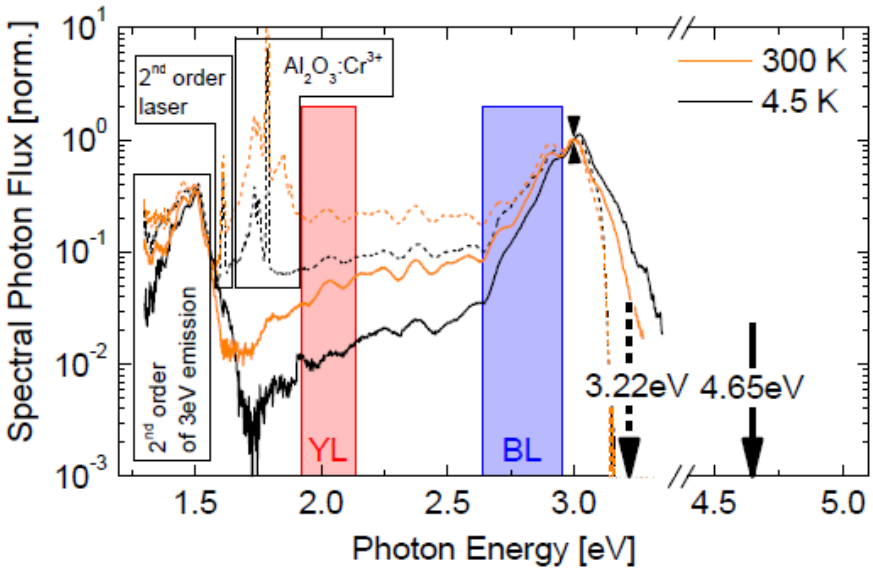

Figure 4-13 PL Spectrum: Sample 1 excited from above using 3.22eV (see footnote 4, page 40)

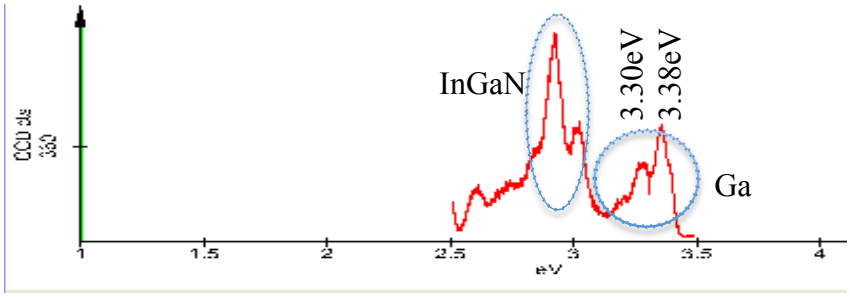

Figure 4-13 PL Spectrum: Sample 1 excited from above using 3.22eV (see footnote 4, page 40)

tensile (subisland) and biaxially compressively strained (free surface) GaN, respectively. These peaks are not seen in the spectrum from use of the 385.5nm (3.22 eV) excitation source, as the excitation source was of lower energy than the GaN bandgap and could not have excited carriers for recombination. Because the 3.22 eV excitation source was of lower energy than the bandgap of GaN, there is only one layer from which the blue-violet (BL) emission (Fig 4-13) could have originated: the InGaN layer. Therefore, the 3 eV

emission peak seen in both spectra must be from lower bandgap InGaN.

4.4.1 Calculating Indium Composition from Emission Data

The indium composition required for the InGaN to luminesce at 3 eV was deduced considering island size, strain, and bond polarity according to the following 4 relationships:

1) Indium composition (redshift with increasing indium) according to Vegard's Law with bowing parameter where $b_{InGaN} = 1.43$ *(34)*

Eq. 13

$$E_{g\,In_xGa_{(1-x)}N} = E_{g\,InN}x + (1-x)E_{g\,GaN} - b_{InGaN}x(1-x)$$

2) Confinement energy (blueshift with decreasing feature size) according to the textbook relation for quantum confinement energy for a quantum disc *(24)*

Eq. 14

$$\Delta E_{g_{QCdisk}} = \frac{h^2}{8m_z d^2} \qquad \frac{1}{m_z} = \frac{1}{m_{e,z}} + \frac{1}{m_{h,z}}$$

3) Strain (blueshift with increasing compressive biaxial strain) according to $\Delta Eg(\varepsilon_{strain})$ relationships from equations 8 and 10 of this paper:

Eq. 15

$$\Delta E_g(\varepsilon_\perp) = b_{g\perp}\varepsilon_\perp\ (eV)$$

$$\Delta E_g(\varepsilon_\parallel) = b_{g\parallel}\varepsilon_\parallel\ (eV)$$

Because there is ambiguity in the interpretation of the lattice parameters of the island deduced from the TEM FFT diffraction pattern, in order to estimate island strain, it was necessary to solve for it assuming a force balance between the island InGaN, and the subisland GaN. Because the c and a strain values of subisland GaN deduced from the TEM FFT diffraction pattern did not correspond to the quasicubic approximation, two separate approaches for calculating island strain and its effect on island InGaN bandgap were evaluated. The two approaches correspond to the above two relations and assume bowing parameters of InGaN are not significantly different from those of GaN.

For the first approach, strain in the c direction in the island was assumed to be equal and opposite to the strain in the c direction in the subisland GaN. The weakness in this approach is that it estimates a tensile biaxial strain in the island, which is opposite what is expected due to In being significantly larger than Ga. This approach estimates strain in the island reduces bandgap and redshifts PL by 0.214eV.

For the second approach, strain in the a direction in the island was assumed to be compressive, equal in magnitude to the sum of absolute values of tensile strain in the a parameter in GaN and the compressive strain value that is standard in GaN grown on sapphire. In this approach, it is assumed that, as the In-rich island grows, strain at the interface due to lattice mismatch is large enough to not only decompress the biaxial plane of subisland GaN, but continue its expansion to eventually bring it to a state of tension. This approach estimates strain in the island increases bandgap and blueshifts PL by 0.105eV.

4) Piezoelectric (QCSE) (redshift with increasing bond polarity in direction of carrier flow) according to the textbook relation ΔEg(ε-field$_{piezo}$) *(1)*:

Eq. 16

$$\Delta E_g^{QCSE} = \frac{C_1(m_e^* + m_h^*)m_0 e^2 \varepsilon_p^2 L_{eff}^4}{\hbar^2}$$

The indium composition in the islands was estimated by equating the sum of the above bandgap relationships to the emission energy measured in the PL tests, then solving for x.

Eq. 17

$$E_{g\,In_xGa_{(1-x)}N} = 0.7x + 3.505(1-x) - 1.43x(1-x) + \frac{h^2}{8m_z d^2} + b\varepsilon + \frac{C_1(m_e^* + m_h^*)m_0 e^2 \varepsilon_p^2 L_{eff}^4}{\hbar^2}$$

5) Stokes (redshift)

As previously mentioned, there is a well-documented difference between bandgap and observed PL, a difference that changes with temperature as well as critical dimensions. In the range of quantum confinement, this difference is reduced. Chichibu et al. *(35)* reported that, for In0.1Ga0.9N QWs of target thickness below 3nm, and tested at 300K, the difference between absorption energy as measured by photoluminescence excitation (PLE) spectra, and low excitation PL emission peak energy was observed to be 50meV. The epi growth time for Samples 1 and 2 of the present study targeted an average layer coverage of 2.5nm, equivalent to a 2.5nm QW with lateral composition fluctuations, with the exception that our samples were not capped with GaN, and the remainder of the device was not fabricated. Stringfellow's 2010 review in the Journal of Crystal Growth (JCG) suggests stokes shift in InGaN/GaN systems can be

attributed to the difference between bandgap as deduced from the average indium composition, and the bandgap of the indium-rich areas (islands) of the film where radiative recombination preferrentially occurs *(36)*. If this is the case, then our calculation to deduce indium composition from PL emission energy should not include a Stokes shift, as we are calculating the indium composition in the preferred radiative recombination areas, not the average indium composition of the entire film.

The resulting values for x, for an emission energy of 3.0eV, calculated according to strain in c lattice parameter, then strain in a lattice parameter, were 7% and 15% indium on the Grp III lattice, respectively (see Appendix A for full calculations).

If we consider individually each peak in the InGaN portion of the spectrum from the PL test using the 3.56 eV source, and if we assume equation 13b applies (calculating the blue-shift due to strain as strictly a function of in-plane strain), then the compositions corresponding to those individual peaks are derived to be 14% and 16%. Due to lattice pulling effects, we know the wetting layer could not possibly contain 14% indium. Below are three possible explanations of the double peak:

- In Stringfellow's 2010 JCG review referred to above, he presents the existence of two peaks in the InGaN emission range as possibly corresponding to opposite ends of the spinode of the phase diagram. If that is the case in this sample, then spinodal decomposition occurred in the islands. The tips and/or cores of the islands are 16% indium, and the

remainder of the body of the islands are 14%. The likelihood of this explanation being true depends on whether the span of composition of the spinode could possibly be so narrow at the strain values achieved for our samples, and at the epi process temp.

- One of the InGaN PL peaks could be emission from islands, the islands having one major mode of indium composition, and the other peak could be emission from the edges or sidewalls of pits, themselves having an indium composition higher than the wetting layer, but also different than the composition indium in the islands. However, there is no supporting evidence in the HRSEM photos of this, as there are no bright, high conductivity outlines to the pits or to the low conductivity areas.
- There could be two modes of InGaN islands, each one with a slightly different indium composition.

4.4.2 PL – Scan Maps

PL scan maps collected by Sebastian Bange using John Lupton's PL test configuration show high intensity blue emission spots most frequently arranged on the edges of much larger, significantly lower intensity yellow emission areas (Fig 4-15). The critical dimension and distribution of yellow emitting areas is consistent with marbling pattern of low conductivity areas shown by HRSEM.

Wide-area PL scan maps from the Witec, with excitation source coming from below the sample and emission collected from above, also show inhomogeneity in intensity, though no change in emission wavelength with travel along the sample (Fig 4-16).

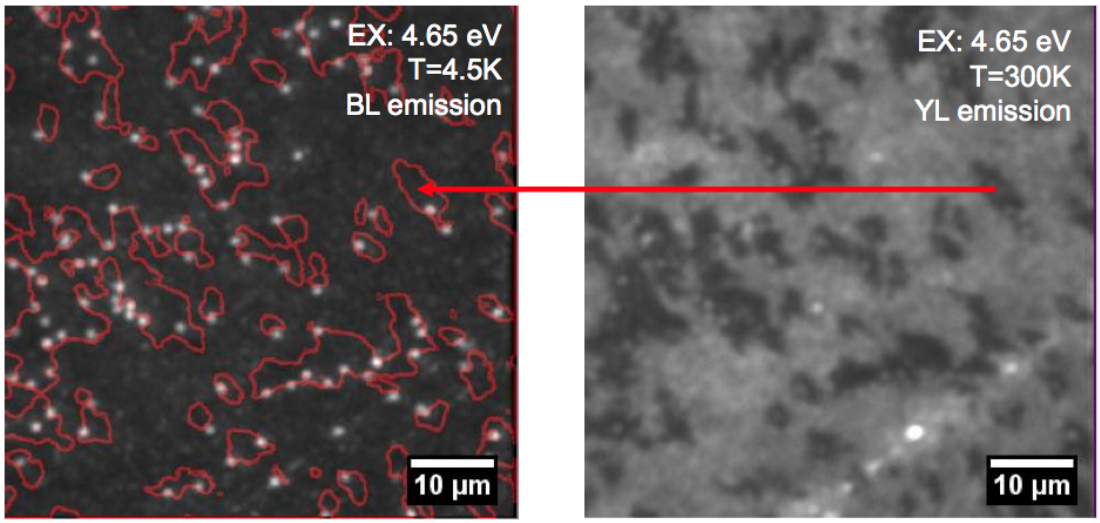

Figure 4-15 PL maps of (left) blue emission spots shown in white positioned at the edges of (right) yellow emitting patches, printed with permission from Sebastian Bange.

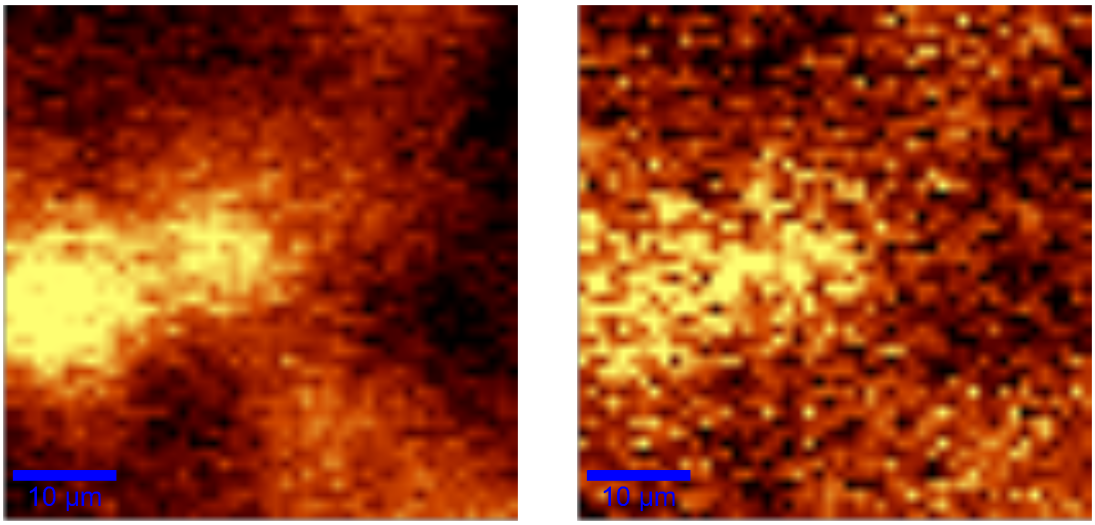

Figure 4-16 Wide-area PL maps of (left) entire emission spectrum and (right) only the peak energy

4.4.3 PL – Emission Polarization

Polarization test results for Sample 1 collected by Sebastian Bange using John Lupton's PL test configuration show bright blue emission spots' polarization ratio > 0.4 (Fig 4-17). This is significant because the emission from unstrained, or perfectly biaxially strained c-plane-grown wurtzite InGaN should not be polarized. The polarization observed from Sample 1's emission could potentially be an indicator of anisotropic biaxial strain.

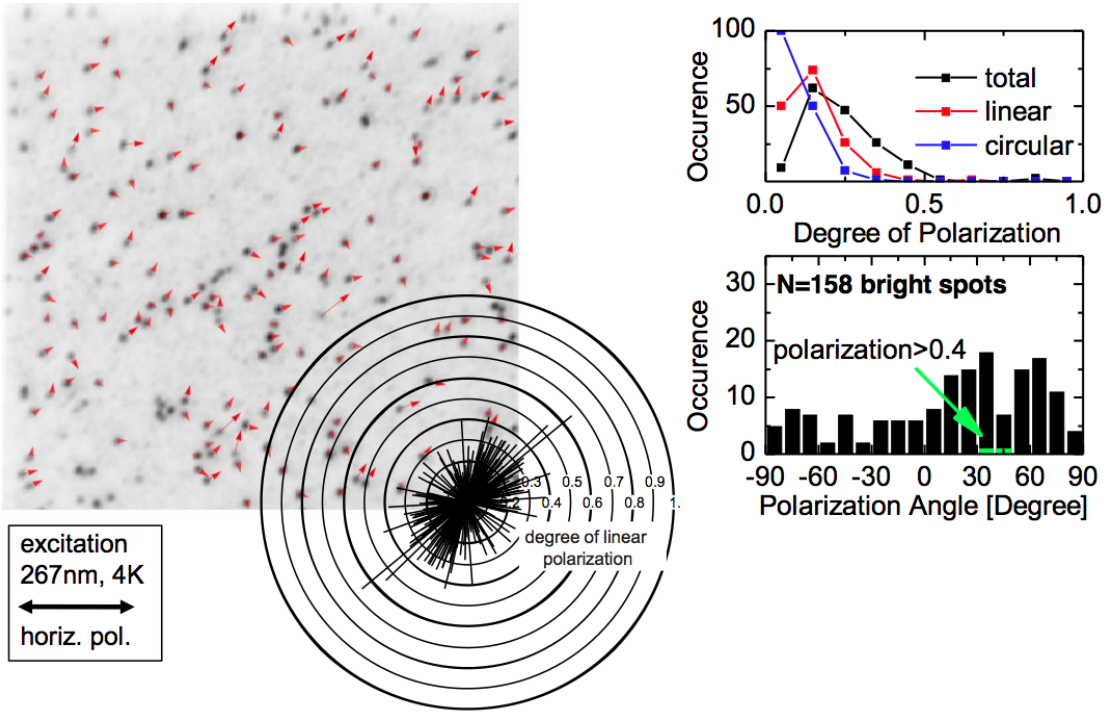

Figure 4-17 Polarization of Emission from Sample 1, printed with permission from Sebastian Bange.

4.4.4 Excitation Source

A 200mW, 405nm laser was tested and emission spectra from Sample 1 were collected by Randy Polson in order to evaluate the possibility of the laser's use as an excitation source for PL testing of Sample 1. Though the 405nm excitation source is of a wavelength between the emission wavelengths of the InGaN and GaN layers and, therefore, theoretically optimal for isolating InGaN emission, it was found to not excite the sample enough to emit, whereas the 5mW 349nm laser does (Fig 4-18). It should be noted that, for use of the 349nm laser in Near-Field testing in Illumination-Collection mode, UV optics and SNOM tips with cores not doped with Ge are required in order to prevent luminescence of the focusing objective and near-field aperture from convoluting collected spectra.

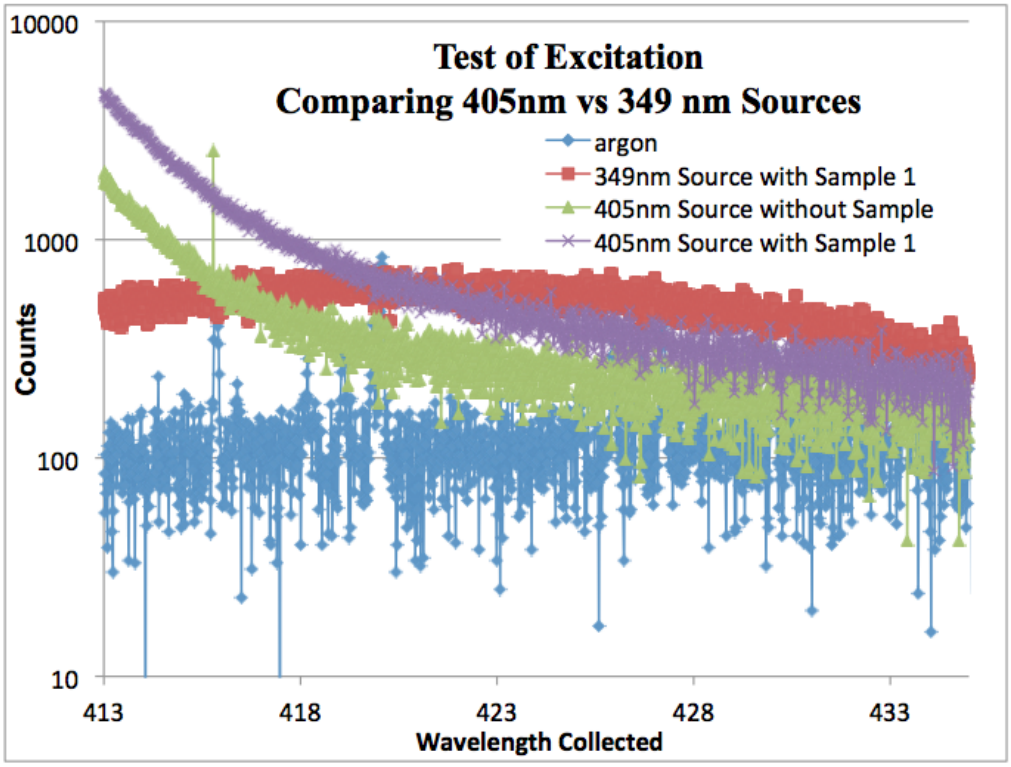

Figure 4-18 Comparing Excitation Sources for use in near-field PL testing of Sample 1.

4.4.5 Near-Field PL Technique

4.4.5.1 Collection Mode

Scanning Near-Field Optical Microscopy (SNOM) was used by Akia Kenata et al., in 2001, to successfully map submicron PL inhomogeneities in an InGaN/GaN sample. With the addition of UV optics (UV objective and polarizing beamsplitter cube), Randy Polson of the U of U Physics Dept. and Laser Dixon Institute was successful in preparing the Witec Alpha-SNOM to execute this test with a UV excitation source, and with confidence that all of the collected spectra were from the sample's emission. None of the collected spectra could be attributed to luminescence from the optics themselves, as the objective and beamsplitter were designed to not luminesce under operation with a UV excitation source.

Our preliminary test evaluating the best equipment configuration for near-field PL showed that exciting from below and collecting through the SNOM tip from above allows collection from outside the SNOM aperture, and changes the resolution of the system to hundreds of microns. Resulting scan maps are, therefore, noise. Exciting and simultaneously collecting through the SNOM tip from above, also referred to as Illumination-Collection mode *(37)*, is the test configuration most likely to maintain nm resolution. However, it is also the configuration that requires the most precise excitation beam alignment, and captures the least overall number of photons, making it the most challenging to successfully execute.

Sample 1 was tested in illumination-collection mode (with excitation from above, and emission collected from above the sample, simultaneously through the SNOM tip) as well as illumination-transmission mode (with excitation from above, through the SNOM tip, and emission collected from below the sample). A 750nm shortpass filter was used

on the collection side to filter reflections from both the 349nm excitation source, and the 900nm feedback laser. The SNOM tip aperture was an oval of about 106nm x 162nm (Fig 4-19).

While the resulting topographic image showed several islands of approximately 10nm height, plus some recessed areas, the photomultiplier tube (PMT) rate image of the same sample area did not show any inhomogeneities in emission intensity (Fig 4-20). This was the case for both illumination-collection and illumination-transmission modes, and was unexpected, as it did not correspond with the PL results from Sample 1 shown in Fig 4-15, nor with published data by the aforementioned Kawakami et al. *(37)* or Soh et al. *(42)* regarding near-field mapping of islanded and pitted samples, respectively. The test was rerun, having stacked a 400nm longpass filter with the 750nm shortpass, in illumination-transmission mode, with no change in resulting emission homogeneity.

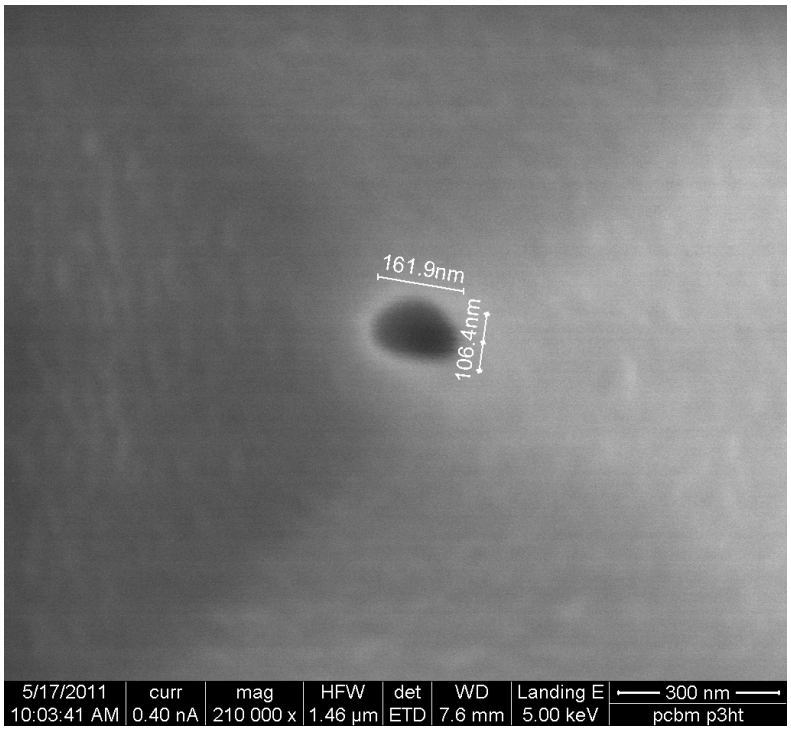

Figure 4-19 SEM image of SNOM tip

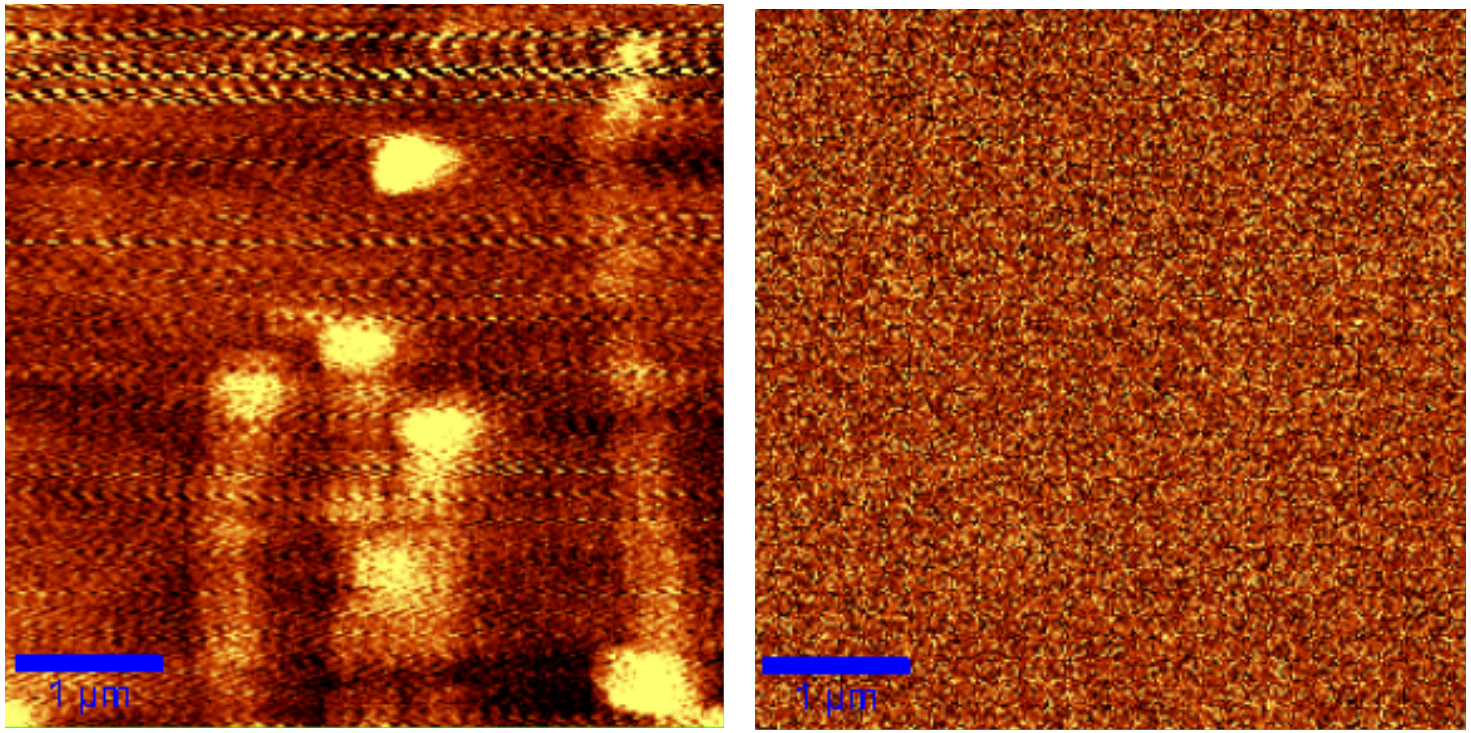

Figure 4-20 SNOM topographical (left) and PMT rate (right) maps for Sample 1; Illumination-Transmission mode. Excitation source: 3.56eV (349nm). SNOM tip aperture: 100x160nm. Image captured while using a 750nm shortpass filter on the collection side.

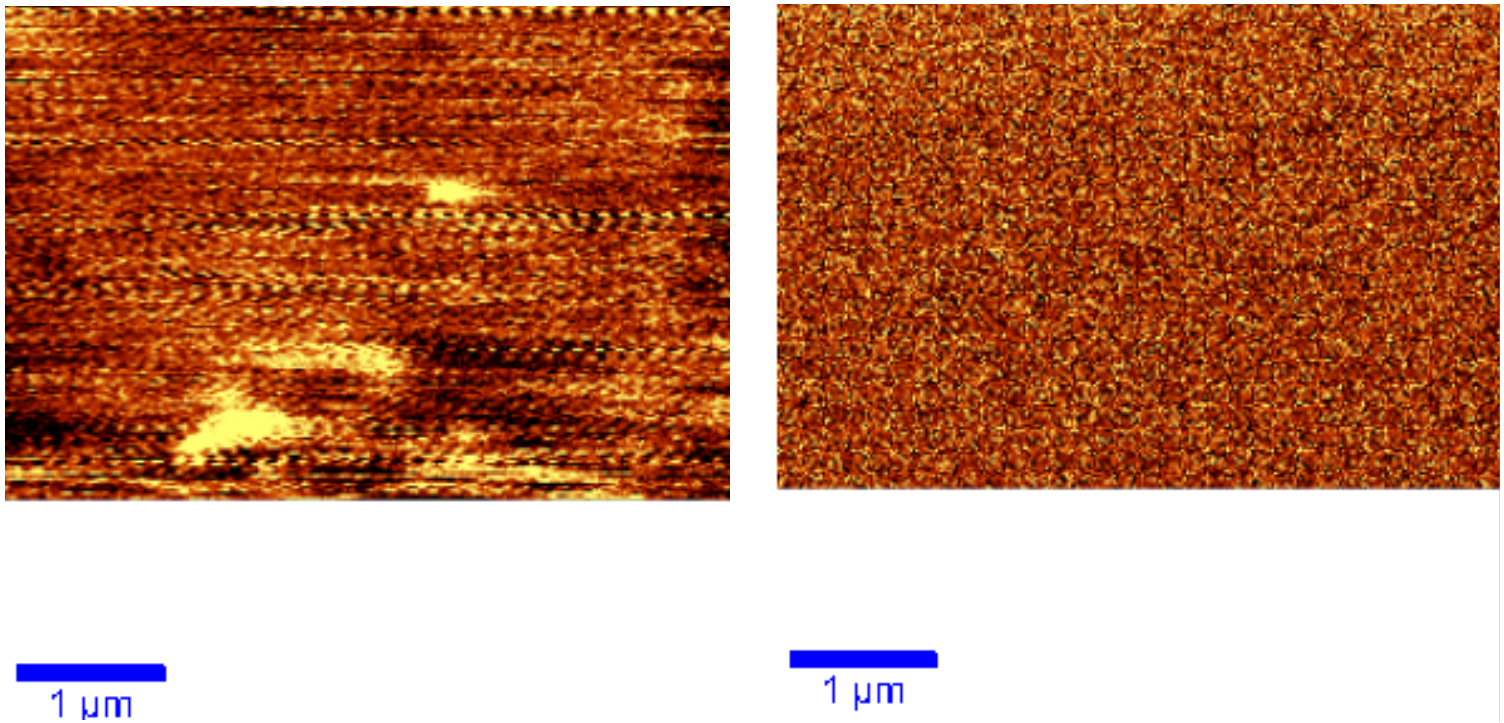

Figure 4-21 SNOM topographical (left) and PMT rate (right) maps for Sample 1; Illumination-Collection mode. Excitation source: 3.56eV (349nm). SNOM tip aperture: 100x160nm. Images captured while using a 750nm shortpass filter on the collection side.

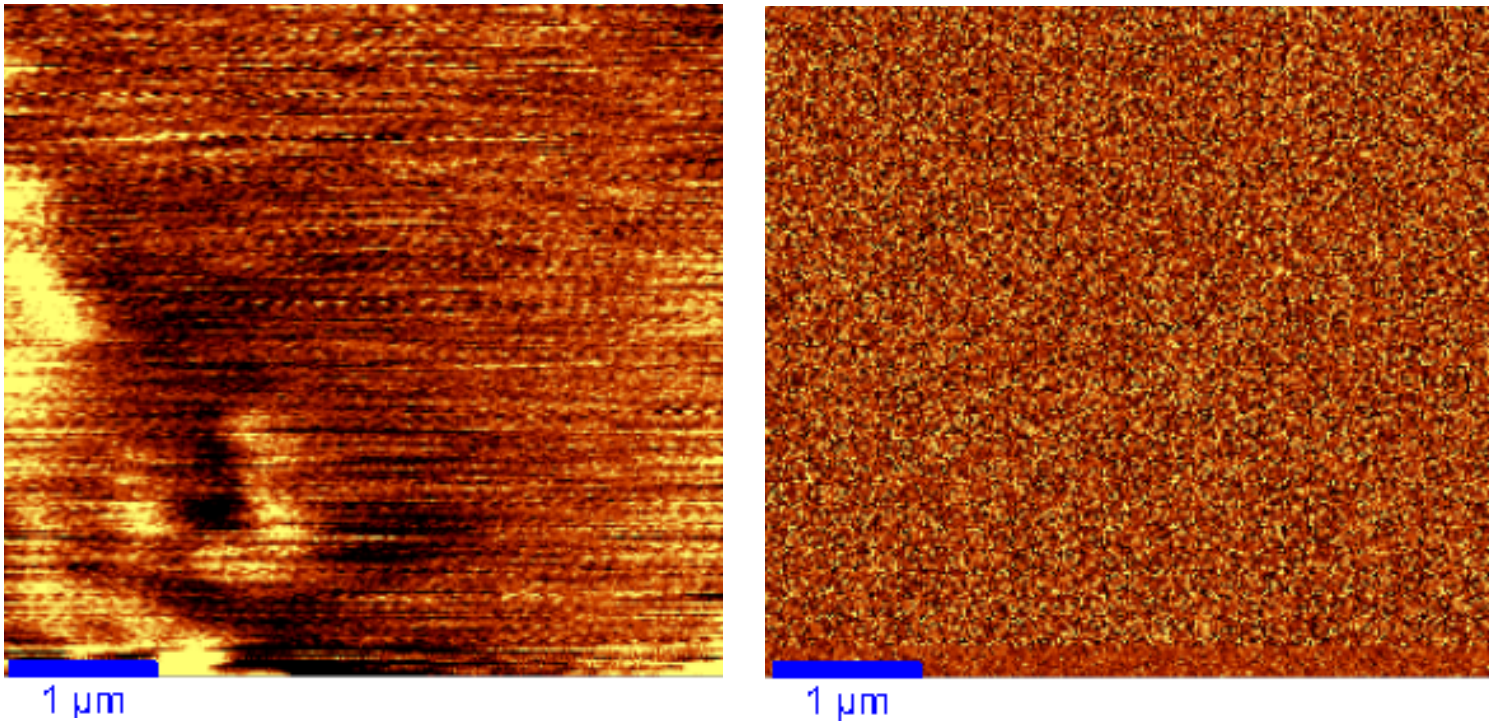

Figure 4-22 SNOM topographical (left) and PMT rate (right) maps for Sample 1; Illumination-Transmission mode. Excitation source: 3.56eV (349nm). SNOM tip aperture: 100x160nm. Images captured while using a 750nm shortpass filter and a 400nm longpass filter, both on the collection side.

Similar to results for Sample 1, PMT rate scans for Sample 2 showed no inhomogeneities (Fig 4-23). Topographic results coincident with this scan are consistent with the AFM scan shown previously (Fig 4-5). No surface features are recognizible. The change in the resolution of the PMT image midscan marks the point at which integration time was increased. The SNOM tip used for this scan was a standard 100nm aperture tip.

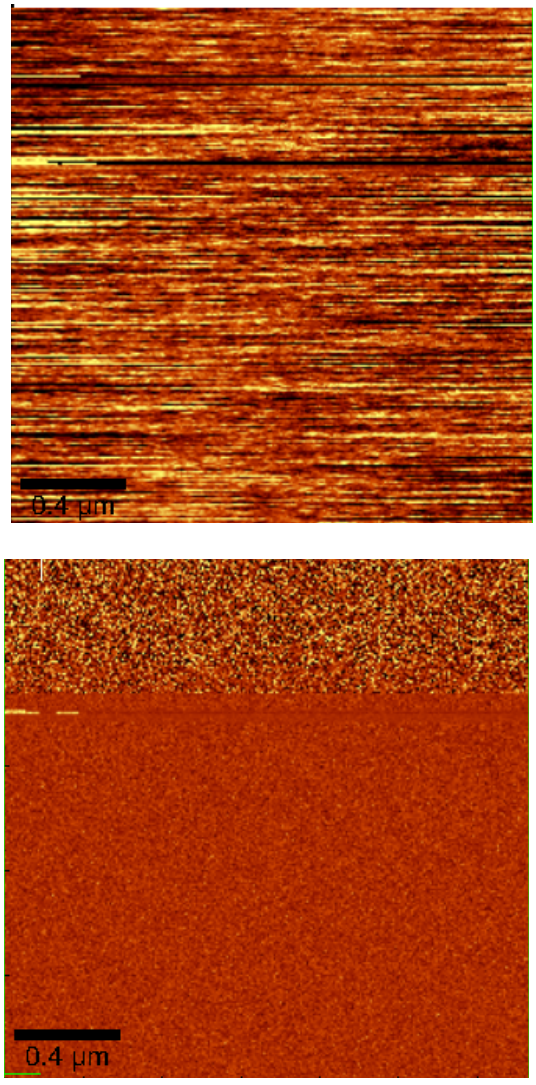

Figure 4-23 SNOM topographical (top) and PMT rate (bottom) maps for Sample 2; Illumination-Transmission mode, using 100nm SNOM tip and 750nm shortpass filter.

4.5 Raman Spectra

For each of Samples 1 and 2, Raman phonon frequencies were plotted (Figs 4-24 and 4-25)[6]. Wurtzite GaN and InxGa1-xN belong to the C^4_{cv} space-group, and their first-order zone-center ($\Gamma = 0$) phonon normal modes are: $2A + 2E1 + 2E2 + 2B1$. Under a 488nm incident beam, the peak A1(LO) and E2 mode frequencies of the two samples were plotted and found to be similar, and consistent with InxGa1-xN on Sapphire. Phonon mode peak frequencies of Samples 1 and 2 were found to be:

$A1(LO)_1 = 751 cm^{-1}$

$A1(LO)_2 = 749 cm^{-1}$

$E2_1 = E2_2 = 575 cm^{-1}$

Published data report A1(LO) and E2 phonon mode frequencies of InxGa1-xN are inversely proportional to increasing indium composition *(38)*. It has also been reported

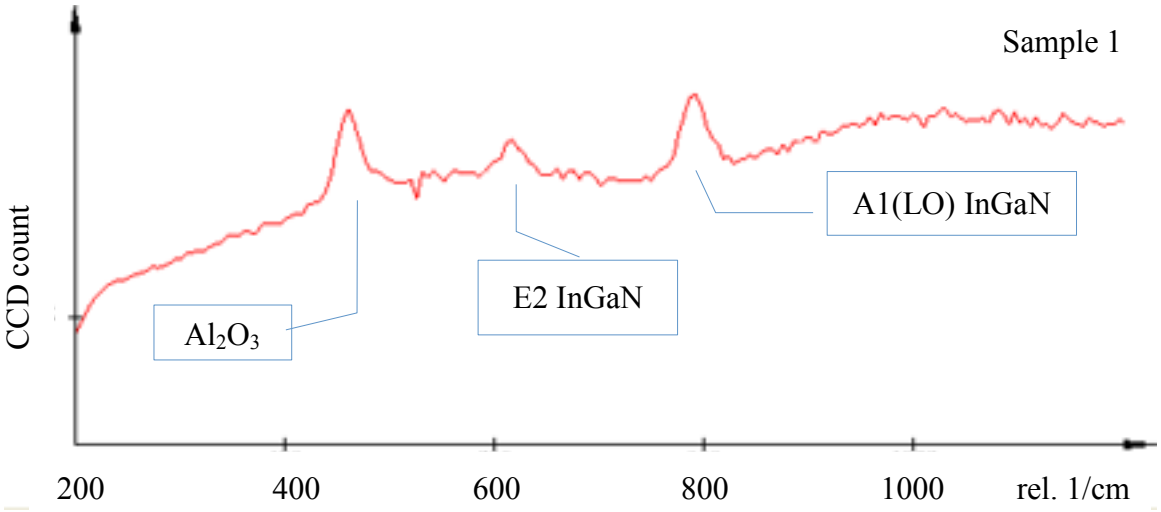

Figure 4-24 Raman plot of CCD counts for peak phonon frequencies from Sample 1 (See footnote 7, this page). The x-axis scale on this image is offset (is high) by 42 cm^{-1}.

[6] Raman spectra collected by Randy Polson, U of U Physics Dept. and Laser Dixon Institute

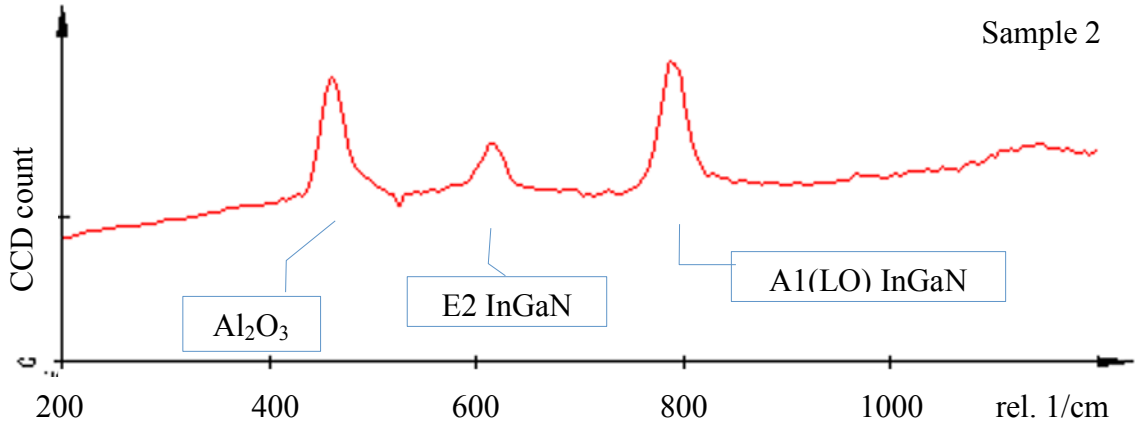

Figure 4-25 Raman plot of CCD counts for peak phonon frequencies from Sample 2 (See footnote 7, page 56). The x-axis scale on this image is offset (is high) by 42 cm^{-1}.

The equation for change in phonon frequency with respect to In composition, including Keating Parameters (*39*):

$$\omega^2{}_{LO}(\Gamma) = \frac{1}{\mu}[4(\alpha+\beta-\sigma)+\frac{2f}{3}] \qquad \textbf{Eq. 18}$$

$$\omega^2{}_{TO}(\Gamma) = \frac{1}{\mu}[4(\alpha+\beta-\sigma)-\frac{f}{3}]$$

The equation for change in phonon frequency with respect to strain, including phonon deformation potentials:

Eq. 19

$$\Delta\omega_{A1} = a_{A1}(\epsilon_{xx}+\epsilon_{yy})+b_{A1}\epsilon_{zz}$$

$$\Delta\omega_{E1,2} = a_{E1,2}(\epsilon_{xx}+\epsilon_{yy})+b_{E1,2}\epsilon_{zz\pm}c_{E1,2}[(\epsilon_{xx}-\epsilon_{yy})^2+4\epsilon_{xy}^2]^{1/2}$$

When strain values are known, the above relationships can be used, along with measured phonon frequencies, to estimate indium composition in InGaN. This was done for our Sample 1, and the calculation can be reviewed in Appendix B. Not unlike the calculation of indium composition from PL data, it was required that this calculation be made more than once, each time with a mutually exclusive assumption:

a. InGaN collective volume (islands and wetting layer, if any) was significant enough to impact the phonon frequency of the underlying and surrounding GaN through its indium composition and strain. Strain in the InGaN, in all three dimensions, is equal and opposite the strain in the underlying GaN. This calculation led to an indium composition estimate of 15-17%.

b. Same as a), except that only strain in the biaxial directions (within the c-plane) is considered. Assuming a balance of forces at the interface between InGaN and GaN, biaxial strain in the InGaN is assumed to be equal and opposite to the deviation of the subisland c-lattice parameter (derived from TEM diffraction pattern measurement), from the value expected for bare GaN/LTGaN/sapphire. This calculation led to an indium composition estimate of 4 to 7%.

c. Any influence of the strain or composition of InGaN islands was overwhelmed by the phonon frequency of the surrounding and underlying GaN. This assumption leads us to the conclusion that the phonon frequencies of Sample 1 match those published for pure GaN/LTGaN/sapphire, with no indium *(38)*.

Whether A1(LO) and E2 phonon frequencies measured for our samples are consistent with a composition of Inx = 15-17%, 4-7%, or 0 is unclear, as the sample volume includes both GaN and InGaN, each with an opposite strain (islands are biaxially compressive and subisland is tensile), and therefore should have an opposite phonon response.

It has been reported that E1 TO and LO and E2 phonon frequencies' splitting would indicate anisotropic distortion in the basal plane *(42)*. We saw no splitting in our preliminary test, though the peak was small. Retesting is necessary to confirm.

Raman can also be used to rule out or confirm the unlikely possibility of the islands being zincblende. Purely wurtzite GaN has a silent B1 phonon mode *(40)*. However, the presence of some zincblend structure in the sample volume results in collection of a frequency peak at $314cm^{-1}$.

5 CONCLUSIONS

5.1 Comparing Sample 1 with Sample 2

Islands and Pits are present on Sample 1, none on Sample 2. Emission intensity from Sample 1 was greater than that of Sample 2. Because no process differences were reported by Cao Group, the provider of those samples, no conclusions can be made regarding the cause of the differences in topography or emission characteristics of the two samples.

5.2 InGaN Layer Topography

Pitting is consistent with the report by Feenstra et al. (2000) of nitrogen vacancy precipitation where the chemical potential difference between the nitrogen molecule, and monatomic nitrogen is the driving force for nitrogen vacancy formation *(41)*.

Eq. 20

$$\Delta \mathrm{E} = -0.1eV + (\mu_N - \mu_{N2})$$

However, it is also possible the pits are evidence of incomplete island coalescence. The occupation of many pits by islands would seem to support this theory. However, other patterns seen in the HRSEM images make this possibility seem less likely due to the presence of pits of significant size near expanses of unpitted areas, and the presence of pits and patterns of pits where no islands are present at all. The incomplete island

coalescence theory does not present an explanation as to the presence of pits without islands.

Island height from Sample 1 almost meets the quantum confinement requirement vertically. Note that this sample's epi growth was interrupted after the InGaN growth step. It is expected that, had it undergone the standard capping process whereby a p-type GaN layer is grown to complete the diode, the island height would have been reduced because InN desorbs faster than GaN under the elevated temperature required for GaN growth, and islands are expected to be In-rich.

High intensity blue emission spots on the edges of larger, lower intensity yellow emission areas as captured in PL measurements correspond in clustering pattern to islands seen in AFM as most often found on the edges or in the deepest portion of pits. Preference of islands to grow at edges and bottoms of pits is consistent with theory that adsorption energy of adatoms during the growth process is lower at or near vacancy locations. Associating the weak yellow emission with pits is consistent with the findings of Soh et al. who used SNOM to map surface pitting of AlInGaN coincident with yellow PL emission *(42)*.

Pits and islands are both nonplanar structures that locally relieve strain in the lattice. SK growth enables InGaN to continue epitaxial growth without continuing to build on the total strain energy held in the lattice wetting layer.

Island and pit densities are not consistent over the entire sample.

5.3 Inhomogeneities on the Order of 5 Micron

Conductivity Inhomogeneities appearing in the HRSEM images are likely composition fluctuation in indium on a large scale that may or may not be coincident with 3D island formation. The inhomogeneity pattern in the YL emission line PL map collected by Sebastian Bange correlates in size and shape with the inhomogeneity pattern in conductivity shown in HRSEM images. Micheletto et al. reported similar inhomogeneities in their near-field PL study of InGaN samples of indium fractions 0.2, 0.25, and 0.3. Of their samples, they found emission intensity to be greatest, and the distance between bright spots lowest with an indium concentration of 0.25. They also concluded that the spatial and optical inhomogeneities of their samples were not uniform within each sample *(43)*. In their SNOM test, the samples were excited through the SNOM tip, and emission was collected on the reverse side (they referred to this as transmission-collection mode).

5.4 Strain - Tensile vs Compressive

Islands are crystalline, and growth is coherent, resulting in tensile strain in the GaN beneath the island, and therefore compressive strain at the base of the island near the interface.

5.5 Island Crystal Structure

There is no likely explanation for the FFT diffraction pattern of Sample 1, Island 1. Two unlikely possibilities are:

5.5.1 Anisotropically biaxially strained m-plane islands growing on c-plane wurtzite

This would seem to require surface reconstruction to satisfy rows of dangling bonds, and evidence of this is not seen in the FFTs (there are no extra spots in the diffraction pattern). Studies analogous, but not identical, to this possibility include c-plane GaN grown on m-plane sapphire *(47)* and the epitaxial habits of zincblende InGaN which sometimes grows perpendicular, and sometimes parallel to, the orientation of the substrate depending on the substrate surface strain condition, a phenomenon the author refers to as the "epitaxial stabilization" effect *(44)*.

5.5.2 Zincblende islands growing on wurtzite GaN

While the Zincblende phase of InGaN has been studied, and a thermodynamic model derived to produce a phase diagram for its substrate-coherent growth on cubic GaN *(45)*, it has not been widely reported as having been grown in thin film or island structures on wurtzite GaN.

Wildeson et al. (2010) reported "zincblende inclusions" at the tips of their $\{1\bar{1}01\}$ faceted, OMVPE-grown, wurtzite GaN pyramids, grown vertically on the c-plane (0001) in the pores of a patterned and etched SiN layer over GaN/sapphire. The zincblende inclusions were confirmed in 9% of nanopyramids grown at 650-780° C, and none of the pyramids grown between 980-1030° C. Wildeson et al. suggest that the presence of zincblende inclusions at the apex of pyramids grown at low temperature can be attributed to lower adatom diffusivity, reducing the probability for achieving the most thermodynamically favorable placement before bonding. Their study included control samples, processed in parallel with the pyramidal samples, with the control samples

grown on non-patterned, planar (0001) GaN/sapphire substrates. TEM analysis showed none of the control samples exhibited zincblende inclusions. This they attributed to the vicinal surface of the substrates, providing low-energy adsorption sites that prevent transition from wurtzitic to zincblende growth. This may seem to explain why the zincblende inclusions were found at the (0001) mesas of the few pyramids that failed to achieve a sharp point during growth. However, it does not well account for the fact that the zincblende inclusions on the pyramids were found at the apex of the sharp-pointed pyramids, and not at the bases.

Zincblende GaN has been reported as having been grown in the LT buffer layer of GaN growing on sapphire, and at a temperature lower than is recommended for high quality crystalline GaN buffer *(14)*. Dhara et al. reported the transformation of GaN from hexagonal to cubic phases in GaN nanowires, but this was observed after Ga+ implantation. They propose two explanatory theories: 1) Ga+ acted as a surfactant, reducing the surface energy, thereby stabilizing the cubic phase, and 2) fluctuations in the short range order induced by enhanced dynamic annealing with irradiation stabilized the cubic phase, causing the transformation *(46)*.

Darachieva et al. *(47)* report Raman Spectroscopy as a method for identifying the presence of cubic GaN as a minor phase in an otherwise wurtzitic GaN film.

5.6 Strain and Emission Polarization

From an historical perspective, it should be stated, here, that a strong polarization of emission (polarization ratio, R = 41.5) has been reported by Lee et al. *(48)* from a different OMVPE-grown III-V system, InGaP. They attribute the cause of this strong polarization to self-assembled composition modulations coincident with surface

undulations (50nm wide, parallel stripes), all brought about by slowing the growth rate, thereby increasing diffusion length and allowing adatoms to rearrange on the surface before being locked into place by subsequent growth. Note that InGaP is a cubic system with symmetry on all three axes, and InGaN is reportedly only stable in the wurtzite structure, which is only biaxially symmetric. Therefore, the physical mechanism for polarization of emission from wurtzitic structures should differ from that of cubic structures.

Polarization of emission from c-plane grown GaN or InGaN is not usual, and is indicative of anisotropic biaxial strain, where instead of there being one a lattice parameter value, there are two distinct a lattice parameter values, distorting the hexagonal structure and further reducing its symmetry. Polarization of emission from wurtzitic GaN has been reported recently by Brinkley et al. for c-plane grown on m-plane *(49)*, thereby inducing anisotropic biaxial strain which rearranges the HH and LH bands in the valence band, making the probability of emission polarized parallel to the growth direction smaller than the probability of emission polarized perpendicular to it.

If the first one of the unlikely scenarios for island crystal structure mentioned previously were true, and islands were wurtzitic, m-plane InGaN grown on c-plane GaN, this would induce the anisotropic biaxial strain, also referred to as anisotropic basal distortion, required for the polarized emission observed in PL testing. It would also explain the two slightly different lattice spacings from the Sample 1, Island 1 FFT, neither of which correspond to the c lattice constant of GaN or InGaN within any published range.

5.7 Indium Composition Estimates

5.7.1 Composition from PL Emission

Accounting for a blue-shift for quantum confinement, another blue shift for island compressive strain, and a redshift for piezoelectric effects (QCSE), the 3 eV emission peak is consistent with $In_xGa_{1-x}N$ of x=0.15. This is consistent with the composition reportedly targeted by actual process conditions.

5.7.2 Composition from Raman-Measured Frequency

Published reports show increasing indium concentrations should decrease the frequency of the A1(LO) and E2 phonon modes. Without considering the effects of strain on the phonon modes as modeled using phonon deformation potentials, then the A1(LO) and E2 peaks of Samples 1 and 2 are consistent with only GaN.

Published reports show tensile strain reduces the frequency of the InGaN and GaN phonon modes, and compressive does the opposite. In Sample 1, we have multiple layers of varying strains. Therefore, in order to most accurately estimate the expected frequency shift due to strain, strain gradients would need to be mapped, fitted to a model, and integrated over the entire sample volume.

Assuming the InGaN island strain to be equal and opposite that measured for the subisland GaN, the indium composition required to compensate for the strain-induced frequency shift of the islands is 15 to 17%. This is consistent with the reported composition targeted by process conditions, and also consistent with composition derived from PL results.

Due to the nature of the assumptions made to use published models to correlate Sample 1 PL and Raman results with the indium composition corresponding to the

reported process target, a third composition analysis technique is required to determine whether PL and/or Raman, or neither, is useful for indium concentration monitoring and can be suggested to industry as an in-line fabrication process control metrology method. Electron Energy Loss Scanning Transmission Electron Microscopy (EELS STEM), as performed by Shumway et al. for the InGaAs system *(50)*, and Scanning Transmission Microscopy (STM) are possible techniques for providing this quantitative, supportive evidence.

5.8 Near-Field Analysis Technique

Using the Physics Dept.'s Witec alpha tool, photoluminescence data, topography data, and Raman data can theoretically all be collected for the same sample area, enabling a correlation of island topography with phonon behavior and emission characteristics that provides a more cogent argument for the cause of emission intensity, and spectra, and patterns observed. That is, carrier excitation and radiative recombination are being directed by composition differences between indium-rich islands that act as quantum dots or discs, and the GaN capping layer to be grown around them.

SNOM test results for InGaN islands in both Illumination-Collection and Illumination-Transmission modes have been published elsewhere and, therefore, are likely reproducible. However, our own tests, to date, have not realized a similar result.

6 RECENT, LATERAL ADVANCES IN INGAN LEDS

Before recommending additional testing, it is requisite that a review of recently published advances be made to ensure the value of future experiments as well as to direct those experiments to build on what has been learned elsewhere from other, critically reviewed studies. The following four studies are outstanding.

6.1 March 2011: GaN Surface Roughening for Polychromatic LED

In this study, InGaN grown on rough GaN surface resulted in In-rich regions of various sizes, each emitting at a wavelength within the Green Gap *(51)*. Roughness was controlled by controlling the temperature of the n-GaN:Si layer as it grew, thereby reducing the diffusion length of Ga adatoms according to:

Eq. 21

$$L^2 = 2D\tau$$

Eq. 22

$$D = D_0 \exp\left(\frac{-E_{A_{Diff}}}{kT}\right)$$

EL test results found three major emission energy modes: 570, 610, and 639nm.

6.2 August 2010: Semipolar, Faceted GaN Pyramids

In this study, Wildeson et al. introduce a porous anodic aluminum (PAA) hardmask and etch process that eliminates the need for nano-lithography in generating a repeating GaN-SiN-GaN pattern through which to grow GaN pyramids that are the substrate providing semipolar $\{1\bar{1}01\}$ facets for growing the InGaN active layer. The reduced crystal polarity in semipolar planes as compared to c-plane increases emission energy through reduced piezoelectric effects. As the average PAA pore size was ~55nm, the base dimensions of subsequently grown GaN nanorods and their GaN pyramid tips were limited by that size. TEM analysis of nearly 3000 features showed the GaN nanorods grown between 980 and 1030°C in the GaN-SiN-GaN patterned layer to be free of dislocations threading from the GaN beneath them, proving the patterned dielectric layer to be an effective dislocation screen. Annular Dark Field (ADF) STEM images of the complete heterostructure show indium-rich InGaN is concentrated at the sharp apex and at the base corners of the pyramids. Samples from this fabrication method showed a *cw*-excited PL, RT/4K emission peak intensity ratio of 0.1 or 10%, which at the time of the publication of this study, was among the highest reported PL ratios from III-Nitrides emitting at greater than 600nm *(52)*.

6.3 February 2011: Single-chip, Phosphor-Free, White-Emitting InGaN/GaN

InGaN QWs are grown on self-assembled, multifaceted GaN islands, enabling different growth rates as well as different indium incorporation on the different facets, resulting in different final thicknesses and concentrations and, therefore, multiple emission energy modes. Controlling GaN island size (Fang et al. reported 1-2 μm

diameter islands in their study) and facets (in their study, they were the semipolar {1 101} , {1 102} , and (0002) atomic planes) as well as QW thickness enables tuning for single-chip polychromatic emission *(53)*.

6.4 April 2011: Nanopatterned Sapphire

Patterning the sapphire substrate via nano-imprint lithography with an array of cylindrical holes of 250nm diameter, then growing GaN, results in voids in the GaN that terminate threading dislocations (TDs). Subsequent growth of InGaN and completion of the LED device using these nanopatterned sapphire substrates results in markedly fewer TDs, and a higher IQE and EQE as compared to the standard, nonpatterned, c-plane sapphire substrate (Fig 6-1) *(54)*.

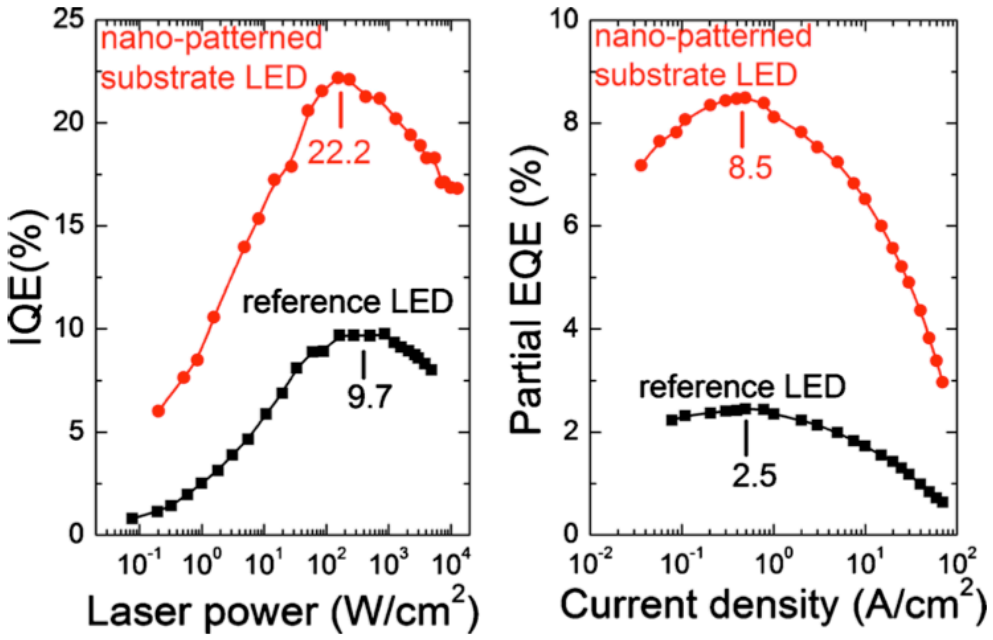

Figure 6-1 IQE as a function of power density (left) and EQE as a function of current density (right) for LEDs fabricated with and without a nanopatterned substrate. Reprinted with permission from C. Wetzel *(54)*.

7 RECOMENDATIONS FOR FURTHER TESTING

7.1 More Samples

Test more samples, this time of known process commonalities and differences, to determine reproducibility of the analysis techniques presented in this report, and extend the meaning of their results.

7.2 SNOM

- For Sample 1, continue efforts to correlate near-field PL with topography of the same sample area, and Raman of the same sample area to prove indium-rich islands are emitting the most intense and longest wavelength photons in the broad emission spectrum, and that blue/violet emitting islands are indeed clustering at the edges of yellow emitting pits or clusters of pits.
- Repeat the same test for Sample 2, showing differences in emission wavelength and intensity as compared to Sample 1, confirming the correlation between surface topography and emission characteristics.

7.3 PL and Polarization Testing

Redo polarization tests using Witec to confirm/support Sebastian's results showing polarization. Test both Samples 1 and 2 and compare. No polarization from Sample 2 would indicate islands and their strains are the source of polarization. Anisotropic strain

in the islands would suggest a growth process cause. Knowing the differences in process conditions between samples would suggest the nature of that cause, and may also explain anisotropy of island sidewall angles.

7.4 EELS STEM

- Confirm indium composition across an island, and on either edge of it. Repeat for other islands.
- Testing along a 5 micron stretch would show whether the inhomogeneities in conductivity seen in HRSEM are indium or nonprecipitated vacancy composition fluctuations. Including an island in that stretch would show whether the large-scale inhomogeneity is exclusive or inclusive of 3D island growth.

7.5 HRTEM FFT

- Test Sample 1, Island 2 to confirm or refute the ZB possibility.
- Calculate lattice parameters of areas of the sample surface without islands to provide a better reference for estimating strain in the bulk GaN, which should be useful in deducing compensating In composition.

7.6 Raman

- Repeat test already done, but use longer collection time and reduce background level. Look for splitting of E2 mode. If splitting of the peak is observed, anisotropic biaxial strain is confirmed.
- Near-field (SNOM) Raman should reduce resolution limit from $\lambda/2$ to $\lambda/10$ to match SNOM PL.

- ZB structure has a B1 phonon mode at 314 cm-1 that is not silent, as compared to the silent B1 mode of the Wurtzite. Retesting with a new orientation of the sample (with photon source perpendicular rather than in parallel to the c-axis of the GaN) would show the silence or lack of B1 phonon mode, proving or disproving ZB possibility.

7.7 AFM

Repeat AFM test while tracking orientation of the sample so as to determine whether pit asymmetry was due to direction of AFM tip travel, or is representative of the actual shape of the pits. This would also explain whether pits sidewall angles are consistently asymmetrical in any one direction, which leads to the question of asymmetrical strain in the GaN.

7.8 HRSEM

- Image Sample 2 to explore composition of the smooth layer. Homogeneity would infer that Sample 1's topography may be linked to composition inhomogeneities.
- Deprocess Samples 1 and 2, removing the InGaN layers, then measure conductivity of the GaN to deduce any Si dopant concentration differences. Map with HRSEM to determine whether Si dopants or N vacancies have coalesced into any particular pattern that corresponds with previously captured conductivity inhomogeneity patterns. This would isolate substrate influence from the influence of InGaN process conditions on resulting conductivity inhomogeneities.

7.9 Surfactant-Assisted Growth Process

- Repeat the entire set of analyses for surfactant-assisted-grown InGaN/GaN on a planar (0001) substrate. Vary surfactant:grp III precursor flow ratio and correlate resulting topography, indium incorporation, and inhomogenity patterns as compared to the results of non-surfactant-assisted growth (compare to this study).
- Run a similar set of tests for surfactant-assisted-grown InGaN/GaN on rough GaN, on GaN grown on nano-patterned sapphire, or on a nano-pyramid-array GaN structure to pursue maximum indium incorporation onto substrates designed to result in simultaneous, multiple-plane growth, and thereby poly-chromatic emission. References for the preparation of these novel substrates are included in Chapter 6 of this paper.

7.10 Dopant Influence on SK-Growth

Evaluate topographic, composition, and emission commonalities for 2.5nm or thinner InGaN/GaN samples having p-type GaN layers of differing dopants and concentrations. Differences in dopants and concentrations should, theoretically, change the surface energy of the substrate on which InGaN is grown, and therefore change the island nucleation and growth process.

APPENDIX A

CALCULATING INDIUM COMPOSITION IN INGAN OF SAMPLE 1 FROM PL EMISSION OF 3.0EV AS A FUNCTION OF STRAIN

This material is attached as supplementary material.

Calculating Indium Composition in InGaN of Sample 1 from PL Emission of 3.0eV as a Function of Strain Either a) Uniaxially or b) Biaxially

a) Uniaxial strain in the islands is assumed to be equal and opposite the uniaxial strain in the sub-island GaN. This calculation results in an Indium composition estimate of 6-7%.
b) Biaxial strain in the islands is assumed to be compressive, and equal in magnitude to the tensile biaxial strain measured in the sub-island minus the compressive biaxial strain expected for bare GaN/LTGaN/sapphire where the a lattice parameter for standard wurtzite GaN/LTGaN/sapphire = 0.31835nm as reported in JApplPhys, 83, 455, Fig2. This calculation estimates Indium composition to be 14-15%.

Indium_x	Eq. 11 *Eg0*	Eq. 12 *deltaEgQC*	Eq. 13a *deltaEgStrainU*	Eq. 13b *deltaEgStrainB*	Eq. 14 *deltaEgQCSE*	Sum of Eqs 12, 13a, 14 *total deltaEg*	Sum of Eqs 11, 12, 13a, 14 *Eg0+total deltaEg*	Sum of Eqs 11, 12, 13b, 14 *Eg0+total deltaEg*
0.01	3.407753	4.80E-02	-0.2136162	9.96E-02	-1.33E-03	-1.67E-01	3.24E+00	3.55E+00
0.02	3.365792	4.81E-02	-0.2136162	9.96E-02	-1.34E-03	-1.67E-01	3.20E+00	3.51E+00
0.03	3.324117	4.82E-02	-0.2136162	9.96E-02	-1.35E-03	-1.67E-01	3.16E+00	3.47E+00
0.04	3.282728	4.83E-02	-0.2136162	9.96E-02	-1.36E-03	-1.67E-01	3.12E+00	3.43E+00
0.05	3.241625	4.84E-02	-0.2136162	9.96E-02	-1.38E-03	-1.67E-01	3.08E+00	3.39E+00
0.06	3.200808	4.85E-02	-0.2136162	9.96E-02	-1.39E-03	-1.67E-01	3.03E+00	3.35E+00
0.07	3.160277	4.86E-02	-0.2136162	9.96E-02	-1.40E-03	-1.66E-01	2.99E+00	3.31E+00
0.08	3.120032	4.87E-02	-0.2136162	9.96E-02	-1.41E-03	-1.66E-01	2.95E+00	3.27E+00
0.09	3.080073	4.88E-02	-0.2136162	9.96E-02	-1.43E-03	-1.66E-01	2.91E+00	3.23E+00
0.1	3.0404	4.89E-02	-0.2136162	9.96E-02	-1.44E-03	-1.66E-01	2.87E+00	3.19E+00
0.11	3.001013	4.90E-02	-0.2136162	9.96E-02	-1.45E-03	-1.66E-01	2.83E+00	3.15E+00
0.12	2.961912	4.91E-02	-0.2136162	9.96E-02	-1.47E-03	-1.66E-01	2.80E+00	3.11E+00
0.13	2.923097	4.92E-02	-0.2136162	9.96E-02	-1.48E-03	-1.66E-01	2.76E+00	3.07E+00
0.14	2.884568	4.93E-02	-0.2136162	9.96E-02	-1.49E-03	-1.66E-01	2.72E+00	3.03E+00
0.15	2.846325	4.94E-02	-0.2136162	9.96E-02	-1.50E-03	-1.66E-01	2.68E+00	2.99E+00
0.16	2.808368	4.96E-02	-0.2136162	9.96E-02	-1.52E-03	-1.66E-01	2.64E+00	2.96E+00
0.17	2.770697	4.97E-02	-0.2136162	9.96E-02	-1.53E-03	-1.65E-01	2.61E+00	2.92E+00
0.18	2.733312	4.98E-02	-0.2136162	9.96E-02	-1.54E-03	-1.65E-01	2.57E+00	2.88E+00
0.19	2.696213	5.00E-02	-0.2136162	9.96E-02	-1.56E-03	-1.65E-01	2.53E+00	2.84E+00
0.2	2.6594	5.01E-02	-0.2136162	9.96E-02	-1.57E-03	-1.65E-01	2.49E+00	2.81E+00
0.21	2.622873	5.03E-02	-0.2136162	9.96E-02	-1.59E-03	-1.65E-01	2.46E+00	2.77E+00
0.22	2.586632	5.04E-02	-0.2136162	9.96E-02	-1.60E-03	-1.65E-01	2.42E+00	2.74E+00
0.23	2.550677	5.05E-02	-0.2136162	9.96E-02	-1.61E-03	-1.65E-01	2.39E+00	2.70E+00
0.24	2.515008	5.07E-02	-0.2136162	9.96E-02	-1.63E-03	-1.65E-01	2.35E+00	2.66E+00
0.25	2.479625	5.09E-02	-0.2136162	9.96E-02	-1.64E-03	-1.64E-01	2.32E+00	2.63E+00
0.26	2.444528	5.10E-02	-0.2136162	9.96E-02	-1.65E-03	-1.64E-01	2.28E+00	2.59E+00
0.27	2.409717	5.12E-02	-0.2136162	9.96E-02	-1.67E-03	-1.64E-01	2.25E+00	2.56E+00
0.28	2.375192	5.13E-02	-0.2136162	9.96E-02	-1.68E-03	-1.64E-01	2.21E+00	2.52E+00
0.29	2.340953	5.15E-02	-0.2136162	9.96E-02	-1.70E-03	-1.64E-01	2.18E+00	2.49E+00
0.3	2.307	5.17E-02	-0.2136162	9.96E-02	-1.71E-03	-1.64E-01	2.14E+00	2.46E+00
0.31	2.273333	5.18E-02	-0.2136162	9.96E-02	-1.72E-03	-1.63E-01	2.11E+00	2.42E+00
0.32	2.239952	5.20E-02	-0.2136162	9.96E-02	-1.74E-03	-1.63E-01	2.08E+00	2.39E+00
0.33	2.206857	5.22E-02	-0.2136162	9.96E-02	-1.75E-03	-1.63E-01	2.04E+00	2.36E+00
0.34	2.174048	5.24E-02	-0.2136162	9.96E-02	-1.77E-03	-1.63E-01	2.01E+00	2.32E+00
0.35	2.141525	5.26E-02	-0.2136162	9.96E-02	-1.78E-03	-1.63E-01	1.98E+00	2.29E+00
0.36	2.109288	5.28E-02	-0.2136162	9.96E-02	-1.80E-03	-1.63E-01	1.95E+00	2.26E+00
0.37	2.077337	5.30E-02	-0.2136162	9.96E-02	-1.81E-03	-1.62E-01	1.91E+00	2.23E+00
0.38	2.045672	5.32E-02	-0.2136162	9.96E-02	-1.82E-03	-1.62E-01	1.88E+00	2.20E+00
0.39	2.014293	5.34E-02	-0.2136162	9.96E-02	-1.84E-03	-1.62E-01	1.85E+00	2.17E+00
0.4	1.9832	5.36E-02	-0.2136162	9.96E-02	-1.85E-03	-1.62E-01	1.82E+00	2.13E+00
0.41	1.952393	5.38E-02	-0.2136162	9.96E-02	-1.87E-03	-1.62E-01	1.79E+00	2.10E+00
0.42	1.921872	5.40E-02	-0.2136162	9.96E-02	-1.88E-03	-1.62E-01	1.76E+00	2.07E+00
0.43	1.891637	5.42E-02	-0.2136162	9.96E-02	-1.90E-03	-1.61E-01	1.73E+00	2.04E+00
0.44	1.861688	5.44E-02	-0.2136162	9.96E-02	-1.91E-03	-1.61E-01	1.70E+00	2.01E+00
0.45	1.832025	5.47E-02	-0.2136162	9.96E-02	-1.93E-03	-1.61E-01	1.67E+00	1.98E+00
0.46	1.802648	5.49E-02	-0.2136162	9.96E-02	-1.94E-03	-1.61E-01	1.64E+00	1.96E+00
0.47	1.773557	5.51E-02	-0.2136162	9.96E-02	-1.96E-03	-1.60E-01	1.61E+00	1.93E+00
0.48	1.744752	5.53E-02	-0.2136162	9.96E-02	-1.97E-03	-1.60E-01	1.58E+00	1.90E+00
0.49	1.716233	5.56E-02	-0.2136162	9.96E-02	-1.99E-03	-1.60E-01	1.56E+00	1.87E+00
0.5	1.688	5.58E-02	-0.2136162	9.96E-02	-2.00E-03	-1.60E-01	1.53E+00	1.84E+00

Constants and Bound Variables			*Reference*
pi	3.14159		
h	4.13565E-15	eV/s	
meGaN	1.8219E-31	kg	Morkoc, Handbook NSD V1
mhGaN	7.2876E-31	kg	Morkoc, Handbook NSD V1
mzGaN-1	6.86E+30	kg-1	derived from above
meInN	1.00205E-31	kg	Morkoc, Handbook NSD V1
mhInN	1.48485E-30	kg	Morkoc, Handbook NSD V1
mzInN-1	1.07E+31	kg-1	derived from above
hbar	6.5821E-16	eV/s	Sze and Ng, SDP
m0	9.1095E-31	kg	Sze and Ng, SDP
e	1.60218E-19	C	Sze and Ng, SDP
RTEg0 GaN	3.45	eV	derived (see text)
RTEg0 InN	0.641	eV	derived (see text)
C1	-0.00219		JLED
GaN ε	10.4		Morkoc, Handbook NSD V2
InN ε	15.3		Morkoc, Handbook NSD V2
wGaN c0	0.5185	nm	Morkoc, Handbook NSD V1
wGaN c	0.5263	nm	measured from FFTs
wInN c0	5.699	nm	APL88, 191918
wGaN a	0.3207	nm	measured from FFTs
wInN a0	0.3535	nm	APL88, 191918
zbGaN a0	0.4511	nm	Morkoc, Handbook NSD V1
zbGaN a	0.47	nm	measured from FFTs
zbInN a0	0.498	nm	Morkoc, Handbook NSD V1
QD height (nm)	7	nm	median island height
QW target thx	2.5	nm	target coverage equivalent
*Stokes for <3nm QW	0.05	eV	APL73, 14 1998

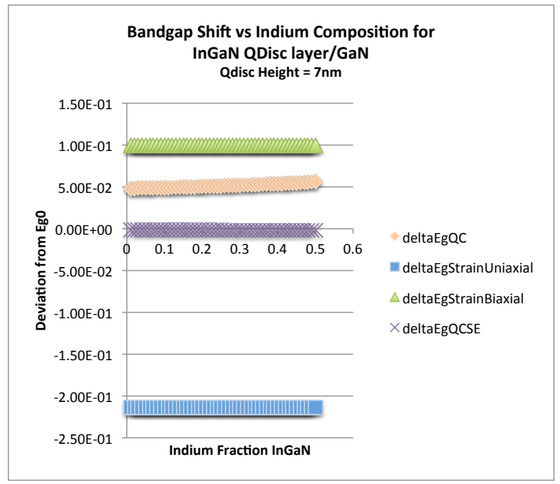

APPENDIX B

CALCULATING INDIUM COMPOSITION IN INGAN OF SAMPLE 1 FROM PHONON FREQUENCIES OF A1(LO) AND E2 MODES AS A FUNCTION OF STRAIN

This material is attached as supplementary material.

Calculating Indium Composition in InGaN of Sample 1 from Phonon Frequencies of A1(LO) and E2 Modes as a Function of Strain

Critical assumptions: InGaN is wurtzite and congruently oriented, in-plane strain is isotropic, and strain is shared at the interface (tension in sub-island is balanced at the interface with compression in island)

Step 1: Tabulating and Plotting Non-Strained A1(LO) and E2 Phonon Frequencies per Eq. 14

Elastic Keating Parameters and Coulomb force constant, f*	Unstrained GaN	Unstrained InN
α	72.89	51.346
β	1.247	-1.247
σ	8.139	3.753
f	163.859	103.36
1/μ	0.086	0.08

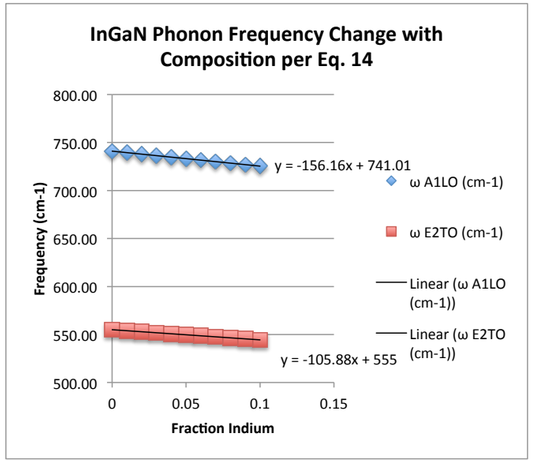

x	M_III	M_N	1/μ	α	β	σ	*f*	ω A1LO (cm^{-1})	ω E2TO (cm^{-1})
0	69.72	14.01	0.09	72.89	1.25	8.14	163.86	741.04	555.03
0.01	70.17	14.01	0.09	72.67	1.22	8.10	163.25	739.46	553.95
0.02	70.62	14.01	0.09	72.46	1.20	8.05	162.65	737.89	552.88
0.03	71.08	14.01	0.09	72.24	1.17	8.01	162.04	736.32	551.82
0.04	71.53	14.01	0.09	72.03	1.15	7.96	161.44	734.75	550.75
0.05	71.98	14.01	0.09	71.81	1.12	7.92	160.83	733.19	549.69
0.06	72.43	14.01	0.09	71.60	1.10	7.88	160.23	731.63	548.64
0.07	72.88	14.01	0.09	71.38	1.07	7.83	159.62	730.07	547.58
0.08	73.33	14.01	0.09	71.17	1.05	7.79	159.02	728.52	546.53
0.09	73.78	14.01	0.08	70.95	1.02	7.74	158.41	726.97	545.48
0.1	74.23	14.01	0.08	70.74	1.00	7.70	157.81	725.43	544.44

M_Ga	69.723
M_In	114.82

Slope (cm-1)/x	
A1(LO)	E2
-156.16	-105.88

Step 2: Calculating Influence of Strain on A1(LO) and E2 Phonon Frequency Shift per Eq. 15

	ω A1LO (cm^{-1})	ω E2 (cm^{-1})
Sample 1	751	575
Sample 2	749	575
Unstrained GaN	750,e 746,b 737g	560,e 567,b 552g
Unstrained InN	596,b 588h	467,b 455h

Deformation Potentials*	Unstrained GaN	Unstrained InN**
a, A1	-846.76	
b, A1	-903.68	
a, E12	-1063.95	
b, E12	-352.08	

	A1LO (cm^{-1})	E2 (cm^{-1})	ε_{xx}	ε_{yy}	ε_{zz}
Sub-island GaN strain from FFTs of Sample 1			0.0058	0.0058	0.015
Δω (ε_{xx})	-4.9112	-6.1709			
Δω (εzz)	-13.5552	-5.2812			
Δω (all)	-23.3776	-17.6230			
Strain of GaN, Full-Thickness of film from FFT of Sample 1				-0.01785	-0.01128
Δω (compressive-xy-only)	15.1147	18.9915			
Δω (all)	25.3082	22.9630			
Strain of GaN Layer (compressive) as expected bare****				-1.19E-03	8.20E-04
Δω (all)	0.2667	0.9775			
Strain of InGaN Layer assuming force balance at interface				-6.99E-03	
Δω (all)	5.9190	7.4371			

Fraction Indium required to Compensate for Δω (strain)

from A1(LO) slope	from E2 slope
If InGaN ε = - GaN ε, xyz	
0.03	0.06
0.09	0.05
0.15	0.17
If InGaN ε = -GaN ε biaxial plus deviation from std.	
0.04	0.07

* Grille, Phys Rev B, 2000. Unstrained GaN A1(LO) and E2 frequency values taken from: aReference 19. bReference 43. cReference 45. dReference 8., eReference 40. fReference 44. gReference 55. hReference 7.
**JApplPhys 108, 123520 (2010)
***InN deformation potentials were assumed to be the same as for GaN
For actual for InN, see Superlattices and Microstructures 36 (2004) 581-589
**** JApplPhys 108, 073522, Zhang

REFERENCES

(*1*) Razeghi, Novel Green Light Emitting Diodes: Exploring Droop-free Lighting Solutions for a Sustainable Earth. Journal of Light Emitting Diodes 2010, 2 (1).

(*2*) Navigant, X. U.S. Lighting Market Characterization; Navigant Consulting and XENERGY for US DOE: 2002.

(*3*) Narukawa, Y.; Ichikawa, M.; Sanga, D.; Sano, M.; Mukai, T., White light emitting diodes with super-high luminous efficacy. Journal of Physics D: Applied Physics 2010, 43 (35), 354002.

(*4*) Nakamura, S., Superbright Green InGaN Single-Quantum-Well-Structure Light Emitting Diodes. Japanese Journal of Applied Physics 1995, 34, L1332-L1335.

(*5*) Krames, M., Shchekin, O., Mueller-Mach, R., Mueller, G., Zhou, L., Gerard Harbers, and Craford, M., Status and Future of High-Power Light-Emitting Diodes for Solid-State Lighting. Journal of Display Technology 2007, 3 (2), 16.

(*6*) Wu, J., LBNL-51260.pdf, DOE OSTI, 2002

(*7*) Ponce, F. A., Appl. Phys. Lett. 80, 550 (2002).

(*8*) Shul, R.J., Solid-State Electronics Volume 42, Issue 12, Dec 98, pp2269-2276

(*9*) Huheey, pps. A-21 to A-34; T.L. Cottrell, "The Strengths of Chemical Bonds," 2nd ed., Butterworths, London, 1958; B. deB. Darwent, "National Standard Reference Data Series," National Bureau of Standards, No. 31, Washington, DC, 1970; S.W. Benson, J. Chem. Educ., 42, 502 (1965).

(*10*) Oya, Fig 1, US Patent 2011/0037089

(*11*) Xu, Y.-N. and Ching, W.Y. (1993) Physical Review B: Condensed Matter, 48, 4335-4350.

(*12*) Dong, Y.; Song, J.-H.; Kim, H.-J.; Kim, T.-S.; Ahn, B.-J.; Song, J.-H.; Cho, I.-S.; Im, W.-T.; Moon, Y.; Hwang, S.-M.; Hong, S.-K.; Lee, S.-W., Raman and emission characteristics of a-plane InGaN/GaN blue-green light emitting diodes on r-sapphire substrates. Journal of Applied Physics 2011, 109 (4), 043103.

(*13*) De Mierry, P.; Guehne, T.; Nemoz, M.; Chenot, S.; Beraudo, E.; Nataf, G., Comparison between Polar (0001) and Semipolar (11\bar22) Nitride Blue–Green Light-Emitting Diodes Grown onc- andm-Plane Sapphire Substrates. Japanese Journal of Applied Physics 2009, 48 (No. 3), 031002.

(*14*) FLORESCU, D.I.; LEE, D.S.; TING, S.M.; RAMER, J.C.; ARMOUR, E.A.; Edge-Emitting Electroluminescence Polarization Investigation of InGaN/GaN Light-Emitting Diodes Grown by Metal-Organic Chemical Vapor Deposition on Sapphire (0001). Journal of Electronic Materials 2003, 32 (11), 5.

(*15*) Stringfellow, G. B., Ho, I-h, Solid phase immiscibility in GaInN. Applied Physics Letters 1996, 69 (18), 2701-2703.

(*16*) Ho, I.-h., Stringfellow, G. B., Solubility of nitrogen in binary III-V systems. Journal of Crystal Growth 1997, 178, 7.

(*17*) Karpov, S.Yu., Suppression of phase separation in InGaN due to elastic strain. MRS Internet Journal of Nitride Semiconductor Research, Vol.3, Art.16, (1998).

(*18*) Falta, J.; Schmidt, T.; Gangopadhyay, S.; Schulz, C.; Kuhr, S.; Berner, N.; Flege, J. I.; Pretorius, A.; Rosenauer, A.; Sebald, K.; Lohmeyer, H.; Gutowski, J.; Figge, S.; Yamaguchi, T.; Hommel, D., Cleaning and growth morphology of GaN and InGaN surfaces. physica status solidi (b) 1-10, 2011. Issue and page numbers not yet assigned.

(*19*) Morkoc, Hadis; Handbook of Nitride Semiconductors and Alloys, Vol 2, p725 Eq 5.116

(*20*) Damilano, B; S. Ve´ zian, N.G.; Massies, J; InGaN heterostructures grown by molecular beam epitaxy: from growth mechanism to optical properties. Journal of Crystal Growth 2001, 227-228, 466-470.

(*21*) Horcas, I.; Fernández, R.; Gómez-Rodríguez, J.M.; Colchero, J.; Gómez-Herrero, J.; and Baro A.M.; Rev. Sci. Inst. 78, 013705 (2007).

(*22*) Sze, S.M.; Ng, Kwok K.; Physics of Semiconductor Devices, Third Edition, Published by John Wiley and Sons, Inc., Hoboken N.J., 2007.

(*23*) Brian E. Foutz, S. K. O. L., Michael S. Shur, Lester F. Eastman, Transient electron transport in wurtzite GaN, InN, and AlN. Journal of Applied Physics 1999, 85 (11), 7727-7734.

(*24*) Morkoc, Hadis, Handbook of Nitrides and Semiconductor Devices, Vol 1, Published by Wiley-VCH Verlag GmbH & Co. KGaA, Weinheim Germany, 2008.

(*25*) Zhang, L.; Cheng, K.; Degroote, S.; Leys, M.; Germain, M.; Borghs, G., Strain effects in GaN epilayers grown on different substrates by metal organic vapor phase epitaxy. Journal of Applied Physics 2010, 108 (7), 073522.

(*26*) Chen, K. P. O. D. a. X., Temperature dependence of semiconductor bandgaps. Applied Physics Letters 1991, 58 (25).

(*27*) Viswanath, A. K., Free Exciton Transitions and Varshni's Coefficients for GaN Epitaxial Layers Grown by Horizontal LP-MOCVD. Solid State Communications 1998, 108 (7), 483-487.

(*28*) Tung, L. T.; Lin, K. L.; Chang, E. Y.; Huang, W. C.; Hsiao, Y. L.; Chiang, C. H., Photoluminescence and Raman studies of GaN films grown by MOCVD. Journal of Physics: Conference Series 2009, 187, 012021.

(*29*) Wu, J,; W. W.; Shan, W.; Yu, K.M.; Ager, J.W. III; Temperature Dependence of the Fundamental Bandgap of InN. LBNL 52113.

(*30*) Zhang, X.; C., S. J.; Liu, W.; Chong, K.-B.; Photoreflectance study of band-gap renormalization in Si-doped GaN. Journal of Crystal Growth 1998, 189/190, 687-691.

(*31*) Schuberta, E.F.; G., I. D.; and Grieshaberb, W.; Optical properties of Si-doped GaN. Applied Physics Letters 1997, 71 (7), 3.

(*32*) Shan, W.; Fischer, A. J.; Hwang, S. J.; Little, B. D.; Hauenstein, R. J.; Xie, X. C.; Kim, D. S.; and Song, J. J.; J. Appl. Phys. 83, 455 (1998).

(*33*) Volm, D.; K. O.; Streibl, T.; Kovalev, D; Ben-Chorin, M.; Diener, J.; and Meyer, B. K.; Exciton fine structure in u-GaN epitaxial films. Physical Review B 1996, 53 (24), 8.

(*34*) Wu, J.; Walukiewicz, W.; Yu, K. M.; Ager, J. W.; Haller, E. E.; Lu, H.; Schaff, W. J., Small band gap bowing in $In_{1-x}Ga_xN$ alloys. Applied Physics Letters 2002, 80 (25), 4741.

(*35*) Chichibu, S. F.; a. A. C. A., Minsky, M. S.; Keller, S.; Fleischer, S. B.; Bowers, J. E.; Hu, E.; Mishra, U. K.; Coldren, L. A.; and DenBaarsb S.P.; Effective band gap inhomogeneity and piezoelectric field in InGaN/GaN multiquantum well structures. Applied Physics Letters 1998, 73 (14), 3.

(*36*) Stringfellow, G. B., Microstructures produced during the epitaxial growth of InGaN alloys. Journal of Crystal Growth 2010, 312 (6), 735-749.

(*37*) Kaneta, A.; Izumi, T.; Okamoto, K.; Kawakami, Y.; Fujita, S.; Narita, Y.; Inoue, T.; Mukai, T.; Jpn. J. Appl. Phys. Vol. 40, (2001) pp110-111

(*38*) Hernández, S.; Cuscó, R.; Pastor, D.; Artús, L.; O'Donnell, K. P.; Martin, R. W.; Watson, I. M.; Nanishi, Y.; Calleja, E., Raman-scattering study of the InGaN alloy over the whole composition range. Journal of Applied Physics 2005, 98 (1), 013511.

(*39*) Schnittler, H. G. a. C., Phonons in ternary group-III nitride alloys. Physical Review B 2000, 61 (9), 6091-6105.

(*40*) Hushur, A.; Manghnani, M. H.; Narayan, J., Raman studies of GaN/sapphire thin film heterostructures. Journal of Applied Physics 2009, 106 (5), 054317.

(*41*) Feenstra, Spontaneous Formation of Indium-Rich Nanostructures on InGaN(0001) Surfaces. Physical Review Letters 2000, 85 (9).

(*42*) Soh, C. B.; Chua, S. J.; Tripathy, S.; Liu, W.; Chi, D. Z., The influence of V defects on luminescence properties of AlInGaN quaternary alloys. Journal of Physics: Condensed Matter 2005, 17 (4), 729-736.

(*43*) Micheletto, R., Indium concentration influence on PL spatial inhomogeneity in InGaN single quantum well structures detected by original low-cost near-field probes. Applied Surface Science 2004, 229 (1-4), 338-345.

(*44*) Liu, J. Z.; Trimarchi, G.; Zunger, A., Prediction of ordering and spontaneous rotation of epitaxial habits in substrate-coherent InGaN and GaAsSb. Applied Physics Letters 2009, 95 (8), 081901.

(*45*) Liu, J.; Zunger, A., Thermodynamic states and phase diagrams for bulk-incoherent, bulk-coherent, and epitaxially-coherent semiconductor alloys: Application to cubic (Ga,In)N. Physical Review B 2008, 77 (20).

(*46*) Dhara, S.; Datta, A.; Wu, C. T.; Lan, Z. H.; Chen, K. H.; Wang, Y. L.; Hsu, C. W.; Shen, C. H.; Chen, L. C.; Chen, C. C., Hexagonal-to-cubic phase transformation in GaN nanowires by Ga[sup +] implantation. Applied Physics Letters 2004, 84 (26), 5473.

(*47*) Darakchieva, V.; Paskova, T.; Schubert, M.; Arwin, H.; Paskov, P.; Monemar, B.; Hommel, D.; Heuken, M.; Off, J.; Scholz, F.; Haskell, B.; Fini, P.; Speck, J.; Nakamura, S., Anisotropic strain and phonon deformation potentials in GaN. Physical Review B 2007, 75 (19).

(*48*) Lee, R. T.; Fetzer, C. M.; Jun, S. W.; Chapman, D. C.; Shurtleff, J. K.; Stringfellow, G. B.; Ok, Y. W.; Seong, T. Y., Enhancement of compositional modulation in GaInP epilayers by the addition of surfactants during organometallic vapor phase epitaxy growth. Journal of Crystal Growth 2001, 233 (3), 490-502.

(*49*) Brinkley, S. E.; Lin, Y.-D.; Chakraborty, A.; Pfaff, N.; Cohen, D.; Speck, J. S.; Nakamura, S.; DenBaars, S. P., Polarized spontaneous emission from blue-green m-plane GaN-based light emitting diodes. Applied Physics Letters 2011, 98 (1), 011110.

(*50*) Shumway, J.; Williamson, A.; Zunger, A.; Passaseo, A.; DeGiorgi, M.; Cingolani, R.; Catalano, M.; Crozier, P., Electronic structure consequences of In/Ga composition variations in self-assembled InxGa1-xAs/GaAs alloy quantum dots. Physical Review B 2001, 64 (12).

(*51*)Park, I.-K., Green Gap Spectral Range Light-Emitting Diodes with Self Assembled InGaN Quantum Dots Formed by Enhanced Phase Separation. Applied Physics Express 2011, 4.

(*52*) Wildeson, I. H.; Colby, R.; Ewoldt, D. A.; Liang, Z.; Zakharov, D. N.; Zaluzec, N. J.; García, R. E.; Stach, E. A.; Sands, T. D., III-nitride nanopyramid light emitting diodes grown by organometallic vapor phase epitaxy. Journal of Applied Physics 2010, 108 (4), 044303.

(*53*) Fang, Z. L.; Lin, Y. X.; Kang, J. Y., InGaN/GaN quantum wells on self-organized faceted GaN islands: Growth and luminescence studies. Applied Physics Letters 2011, 98 (6), 061911.

(*54*) Li, Y.; You, S.; Zhu, M.; Zhao, L.; Hou, W.; Detchprohm, T.; Taniguchi, Y.; Tamura, N.; Tanaka, S.; Wetzel, C., Defect-reduced green GaInN/GaN light-emitting diode on nanopatterned sapphire. Applied Physics Letters 2011, 98 (15), 151102.